Comparing Normal Modes Across Different Models and Scales: Hessian Reduction *Versus* Coarse-Graining

An Ghysels,*[a] Benjamin T. Miller,*[b] Frank C. Pickard IV,[b] and Bernard R. Brooks[b]

Dimension reduction is often necessary when attempting to reach longer length and time scales in molecular simulations. It is realized by constraining degrees of freedom or by coarse-graining the system. When evaluating the accuracy of a dimensional reduction, there is a practical challenge: the models yield vectors with different lengths, making a comparison by calculating their dot product impossible. This article investigates mapping procedures for normal mode analysis. We first review a *horizontal* mapping procedure for the reduced Hessian techniques, which projects out degrees of freedom. We then design a *vertical* mapping procedure for the 'implosion' of the all-atom (AA) Hessian to a coarse-grained scale that is based upon vibrational subsystem analysis. This latter method derives both effective force constants and an effective kinetic tensor. Next, a series of metrics is presented for comparison across different scales, where special attention is given to proper mass-weighting. The dimension-dependent metrics, which require prior mapping for proper evaluation, are frequencies, overlap of normal mode vectors, probability similarity, Hessian similarity, collectivity of modes, and thermal fluctuations. The dimension-independent metrics are shape derivatives, elastic modulus, vibrational free energy differences, heat capacity, and projection on a predefined basis set. The power of these metrics to distinguish between reasonable and unreasonable models is tested on a toy alpha helix system and a globular protein; both are represented at several scales: the AA scale, a Gō-like model, a canonical elastic network model, and a network model with intentionally unphysical force constants. Published 2012 Wiley Periodicals, Inc.†

DOI: 10.1002/jcc.23076

Introduction

To reach longer length and time scales in simulations, molecular systems are often treated with different levels of detail. As every atom can perform translations in three directions, a molecular system with N_A atoms has $3N_A$ degrees of freedom, which becomes computationally challenging as system size increases. The dimensionality can be reduced by constraining some degrees of freedom or using a model with fewer interaction centers. This can lead to a reduction in both CPU time and memory usage.[1–3] The first mechanism retains the number of atoms but constrains the atomic motion. The second mechanism, known as coarse-graining, groups atoms into N_{CG} beads, where $N_{CG} \ll N_A$. An important question is how the change in dimensionality affects the vibrational motions of the system, which are calculated via normal mode analysis (NMA).

NMA is a technique to calculate the vibrational spectra of molecular systems.[4] The procedure starts with a geometry optimization to obtain a stationary energy point on the potential energy surface. The Hessian matrix is then constructed by taking the second derivatives of the potential energy with respect to the nuclear displacements. Finally, mass-weighting and diagonalizing the Hessian yields a set of eigenvalues and eigenvectors, which correspond to the frequencies and normal modes, respectively. As a consequence of the modeling at multiple scales, the number of frequencies as well as the length of the mode vectors can vary between different levels of detail. The different sizes of the normal modes prevent a facile comparison of the scales by taking their dot product. This article aims to address the practical question of how normal modes and frequencies should be compared between the different scales and which metrics are most effective in evaluating the quality of a model.

NMA reveals properties of a molecular system that may be useful for determining its biological and chemical function. For example, it is used to calculate the infrared spectrum of organic compounds, facilitating the interpretation of experimental spectra. NMA may also be used to verify if a structure is optimized to a local minimum or a transition state. In chemical kinetics, the frequencies of the reactants and the transition state serve as the input for the vibrational partition function, from which the vibrational free energy contribution to the reaction constant[5] or the kinetic isotope effect[6] can be derived. In biological systems, 90% of the large-amplitude motions related to conformational change, and thus biological function, are found to be among the lowest 10 vibrational modes in many investigated proteins.[7–10] Normal modes are also useful in predicting conformational changes based on iterative mode-tracking algorithms.[11]

[a] *A. Ghysels*
Center for Molecular Modeling, Ghent University, Technologiepark 903, 9052 Gent, Belgium
E-mail: an.ghysels@ugent.be
[b] *B. T. Miller, F. C. Pickard IV, B. R. Brooks*
Laboratory of Computational Biology, National Heart, Lung, and Blood Institute, National Institutes of Health, Bethesda, Maryland 20892
E-mail: btmiller@nhlbi.nih.gov

Contract/grant sponsor: Intramural Research Program of the NIH, National Heart, Lung and Blood Institute.

In all these examples, it is important to validate whether a constrained or coarser model still captures the essential information of the NMA. As mentioned, the dimensionality may be reduced by two mechanisms. The first is constraining or integrating out certain degrees of freedom, which we refer to as reduced Hessian techniques. The second is coarse-graining a molecular system, to arrive at a description of interacting particles. As there are fewer interaction centers in the coarse-grained (CG) model than in the original all-atom (AA) model, the number of frequencies and the length of the normal modes are smaller. Figure 1 illustrates the

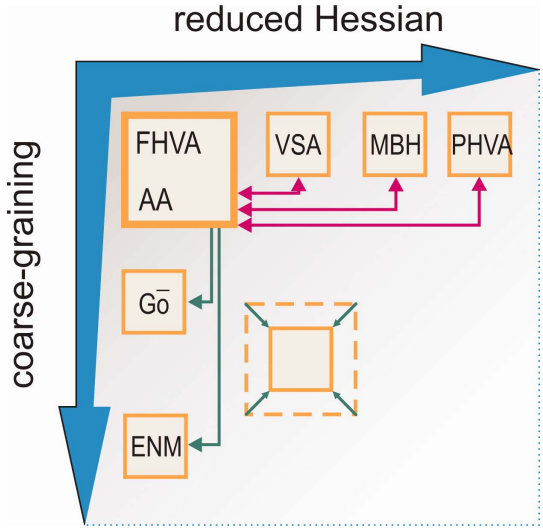

Figure 1. The relationship between various reduced dimension Hessians. The largest Hessian is the full Hessian at the AA scale (AA/FHVA). Horizontal mapping is needed to match the sizes for reduced Hessian techniques (VSA, MBH, and PHVA). Vertical mapping is needed for comparison of coarse-grained scales (Gō, ENM) and is realized by 'imploding' the AA Hessian to the CG size. [Color figure can be viewed in the online issue, which is available at wileyonlinelibrary.com.]

reduced Hessian techniques (on the horizontal axis) and the CG schemes (on the vertical axis) used in this article.

On the horizontal axis of Figure 1, the standard method is the full Hessian vibrational analysis (FHVA). The FHVA diagonalizes the full mass-weighted Hessian, implying that all atoms, or beads, participate in the vibrational motion. The partial Hessian vibrational analysis (PHVA)[12–14] treats only the subsystem of interest as mobile, whereas the rest of the system is immobilized. This approach effectively assigns an infinite mass to the immobile atoms. For instance, when modeling surface adsorption, this technique could constrain the bulk material, whereas only the first few layers of the crystal participate in the vibrations.[15] In the mobile block Hessian (MBH) method,[16,17] parts of the system are treated as mobile rigid blocks with a finite mass and finite moments of inertia, keeping the internal geometry of each block fixed while other atoms are still allowed to vibrate individually. For instance, when modeling proteins, the CH bond stretches of the side chain are thought to be unimportant in large-scale conformational changes, so these are fixed.[18] The equivalent of this dimension reduction is the SHAKE algorithm in molecular dynamics.[19] The MBH is essentially the same method as the rotation-translation block (RTB) method,[20–22] but MBH is designed to also treat partially optimized systems by including an additional gradient correction term.[17] Moreover, the MBH formalism has been extended to the case of linked blocks, which can have an atom or a pair of atoms in common.[18,23] In the vibrational subsystem analysis (VSA)[24–26] method, the system is partitioned into a subsystem and an environment. The vibrations of the subsystem are calculated, but under the specific condition that the subsystem is adiabatically coupled to the environment.

All of these methods (PHVA, MBH/RTB, and VSA) are *in se* based on the projection of the full $3N_A$ configurational space onto a subspace by means of a reduced basis set, the exception being MBH because of the additional gradient correction term in partially optimized structures. The effect of this projection has been extensively studied.[16,27] Other reduced basis sets have also been proposed. Because backbone dihedral angles are critical for the description of protein dynamics, several studies have used this basis to investigate protein flexibility.[28–30] Other studies have used spherical harmonics (SH) in conjunction with backbone dihedral functions to identify global shape deformations,[29] and the combined PHVA-MBH approach has been developed to model zeolite adsorption[31] and identify adsorbate and framework vibrations of porous crystals.[32]

On the vertical axis of Figure 1, the most detailed scale is the AA description with N_A interaction centers. Although we chose to use molecular mechanics (MM) methods in this work, one could also apply our Hessian methods to both quantum mechanical (QM) and hybrid QM/MM studies.[33–35] Note that a complete QM/MM analytical Hessian matrix is now available in the CHARMM and Q-Chem implementation.[35]

Less detail is included in CG models that describe the molecule as a set of beads. There are many ways to parametrize the interactions between these particles. Examples are fitting to data from AA calculations[36–38] and fitting to experimental data such as melting temperatures.[39,40] Where a full Hessian diagonalization of an AA description is computationally intractable, a reduced Hessian analysis at a CG scale may still be possible. Because of their smoother potentials, CG models sample their conformational space more efficiently than their AA counterparts, which may be hampered by nonergodicity. A comprehensive overview may be found in Tozzini.[41]

An example CG force field is the elastic network model (ENM) for proteins.[42,43] Each residue is represented by a bead at the alpha-carbon (C_α) position, which interacts through harmonic bonds (springs) with neighboring beads within a specified cut-off radius. This simple description captures a considerable part of the slow dynamics.[44,45] Modifications of the ENM may alter the masses[42] or may optimize the force constants of the springs from AA molecular dynamics simulations.[46] In the Gaussian network model (GNM), the harmonic bond terms are independent of the direction in which the bond is stretched, which implies isotropic and Gaussian distributed fluctuations of the particle coordinates.[43,47] In the anisotropic network model (ANM), which is equivalent to the standard

ENM, the interaction is dependent on the direction in which the particles are displaced.[48] In a hybrid model, the ANM (ENM) and GNM are unified in the framework of a generalized ANM (G-ANM), where the degree of direction-dependent interactions is tuned with an anisotropy parameter.[49] A different approach is used by Gō-like models.[50] The residues are represented by beads, but a new set of parameters has to be constructed for every new structure, making a Gō model not transferable between structures. The Gō model in this article is based on the work of Klimov and Thirumalai and henceforth will be called the KT model.[39,51,52]

This article provides a suite of metrics for mode comparison at different scales. Some of these metrics are dimension-dependent, meaning that the direct comparison between modes and frequencies of different dimension is not possible. To resolve this problem, we use horizontal mapping for reduced Hessian techniques and we develop a vertical mapping procedure for CG models. Section Horizontal mapping for reduced basis sets describes how horizontal mapping uses a reduced basis set to construct a projection matrix. In section Vertical mapping for coarse-grained models, we propose a vertical mapping procedure between scales of different resolution based on VSA, using a set of generalized coordinates. These coordinates are chosen to represent the CG particles, such that the high-resolution Hessian is "imploded" to a Hessian containing effective force constants for the generalized coordinates. We refer to this smaller Hessian as the imploded Hessian, which has the same size as the low-resolution Hessian, facilitating normal mode comparison. The concept of Hessian implosion was first proposed by Eom, Zhou, and coworkers,[53,54] but a systematic treatment of the masses was not performed. In our VSA framework, the kinetic tensor (mass matrix) is also imploded, so that the inertia of the molecular system is correctly taken into account.

An alpha helix (section Test Cases: Alpha Helix and Globular Protein) and the albumin-binding domain of protein G (section Illustration with a Globular Protein) are used as test examples. These are modeled with an AA force field and with three CG force fields: a Gō-like model (KT), an ENM with plausible force constants, and an ENM with unphysical force constants, referred to as the horrible network model (HNM). The latter model serves as a negative control and enables us to test whether the metrics discriminate between "good" and "bad" CG models.

Section Metrics presents the quantities that are the direct result of NMA: frequencies and normal modes. Next, various derived metrics are presented: thermal fluctuations, probability similarity, Hessian similarity, collectivity of modes, shape derivatives, spherical harmonics, elastic modulus, difference in vibrational free energy, and heat capacity. The truly dimension-independent metrics are shape derivatives, spherical harmonics, elastic modulus, heat capacity, and difference in vibrational free energy. For all other metrics, a prior mapping should be performed according to the procedures described in sections Horizontal mapping for reduced basis sets and Vertical mapping for coarse-grained models. Finally, we conclude with a summary evaluation of the metrics' effectiveness in section Conclusions, which may serve as a practical guide when comparing reduced Hessian techniques or coarse-grained models.

Mapping

Assume the Cartesian positions of the N_A atoms are denoted by a $3N_A$-dimensional vector r_i. The full Hessian is the $3N_A \times 3N_A$ symmetric matrix containing the second derivatives of the potential energy with respect to atomic positions,

$$H_{i,j}^{\mathrm{AA}} = \left(\frac{\partial^2 E^{\mathrm{AA}}}{\partial r_i \partial r_j}\right)_0 \tag{1}$$

evaluated at a reference point r_i^0. The Hessian is positive semidefinite in a minimum energy state, meaning that any atomic displacements would increase the potential energy. A few coordinates exist where the potential energy stays constant due to invariances, that is, rotation and translation of the entire system, leading to six (five if the molecule is linear) zero frequencies in the subsequent NMA.[17] Before diagonalization, the Hessian is mass-weighted with a kinetic tensor matrix, which is positive definite. For the FHVA, this matrix is a $3N_A \times 3N_A$ diagonal matrix with the atoms' masses on the diagonal,

$$M_{i,j}^{\mathrm{AA}} = \delta_{ij} m_i. \tag{2}$$

The $3N_A$ frequencies ω^{AA} and normal modes v^{AA} of length $3N_A$ are then obtained by solving the generalized eigenvalue problem,

$$H^{\mathrm{AA}} v^{\mathrm{AA}} = (\omega^{\mathrm{AA}})^2 M^{\mathrm{AA}} v^{\mathrm{AA}}. \tag{3}$$

All eigenvalues $(\omega^{\mathrm{AA}})^2$ are non-negative in a minimum energy state, whereas at least one eigenvalue is negative in a transition state, leading to an imaginary frequency. Similar equations hold when the dimensionality is changed using reduced basis sets ($H^{\mathrm{re}} v^{\mathrm{re}} = (\omega^{\mathrm{re}})^2 \mathrm{M}^{\mathrm{re}} v^{\mathrm{re}}$) or using CG models ($H^{\mathrm{CG}} v^{\mathrm{CG}} = (\omega^{\mathrm{CG}})^2 \mathrm{M}^{\mathrm{CG}} v^{\mathrm{CG}}$).

Ideally, one would directly compare the results of the NMA: frequencies, normal modes, and Hessians, but the different dimensionality makes this task nontrivial. The challenge is comparing a different number of frequencies and normal modes arising from the differently sized Hessians. For direct comparison, it is therefore necessary to find mappings between the different scales shown in Figure 1. To map a lower dimensional scale to a higher dimensional scale, two approaches can be used: expand the smaller Hessian to a larger one by adding information or shrink the larger Hessian to a smaller one by projection. Adding information is an arbitrary process; therefore, the most acceptable approach is projecting larger Hessians into the smaller Hessians.

Alternatively, one can use quantities derived from the normal modes and frequencies, such as B-factors or the elastic modulus. Many of these derived quantities can be directly tied back to experiment. Some of them have the advantage that they are dimension-independent, making prior mapping

unnecessary. For instance, the elastic modulus, which quantifies the rigidity of a molecule with respect to strain, is calculable at every scale, and thus is easy to compare between scales. In contrast, a B-factor profile plots the average fluctuation of each particle, so a mapping between the scales has to be established before the profiles are compared. The following two subsections describe methods for mapping between the different scales on the horizontal and vertical axes of Figure 1.

Horizontal mapping for reduced basis sets

When using a reduced basis set, the dimensionality of the NMA is decreased by projecting the $3N_A$ space onto a smaller subspace of dimension m, for instance consisting of block motions (MBH). The original Cartesian coordinates r_i, $i = 1,\ldots,3N_A$, are a function of the m reduced basis set coordinates q_α, $\alpha = 1,\ldots,m$: $r_i = r_i(q)$. Both the full Hessian and the mass matrix are projected onto a $3N_A \times m$ matrix P, whose columns are the vectors of the reduced basis,

$$H^{\mathrm{re}} = P^T H^{\mathrm{AA}} P \tag{4}$$

$$M^{\mathrm{re}} = P^T M^{\mathrm{AA}} P. \tag{5}$$

Projection yields the reduced Hessian H^{re} and reduced mass matrix M^{re} of dimension $m \times m$. For an optimized structure, H^{re} contains the second derivatives of the energy with respect to the q coordinates,

$$H^{\mathrm{re}}_{\alpha,\beta} = \left(\frac{\partial^2 E^{\mathrm{AA}}}{\partial q_\alpha \partial q_\beta}\right)_0 = \sum_{ij}\left(\frac{\partial^2 E^{\mathrm{AA}}}{\partial r_i \partial r_j}\right)_0 \left(\frac{\partial r_i}{\partial q_\alpha}\right)_0 \left(\frac{\partial r_j}{\partial q_\beta}\right)_0 \tag{6}$$

evaluated at the reference point. The elements $P_{i\alpha}$ are equal to $(\partial r_i/\partial q_\alpha)$. Solving the generalized eigenvalue problem,

$$H^{\mathrm{re}} v^{\mathrm{re}} = (\omega^{\mathrm{re}})^2 M^{\mathrm{re}} v^{\mathrm{re}} \tag{7}$$

yields m frequencies and m normal mode vectors of length m. M^{re} might be nondiagonal, which makes the mass-weighting of the Hessian more involved. As M^{AA} is positive definite, the projected matrix $P^T M^{\mathrm{AA}} P = M^{\mathrm{re}}$ is also positive definite. Therefore, the square root of M^{re} exists and can be constructed by diagonalizing M^{re}, so eq. (7) is equivalent to

$$\tilde{H}^{\mathrm{re}} \tilde{v}^{\mathrm{re}} = (\omega^{\mathrm{re}})^2 \tilde{v}^{\mathrm{re}} \tag{8}$$

with the mass-weighted reduced Hessian $\tilde{H}^{\mathrm{re}} = (M^{\mathrm{re}})^{-1/2} H^{\mathrm{re}} (M^{\mathrm{re}})^{-1/2}$ and mass-weighted reduced eigenvectors $\tilde{v}^{\mathrm{re}} = (M^{\mathrm{re}})^{1/2} v^{\mathrm{re}}$.

The reduced basis set need not be a linear combination of the Cartesian coordinates. For instance, the spherical harmonics depend nonlinearly on the Cartesian coordinates. Only the linearized dependence appears in the normal mode equations. For instance, from the relation

$$r_i = r_i^0 + \sum_\alpha \left(\frac{\partial r_i}{\partial q_\alpha}\right)_0 \Delta q_\alpha + \frac{1}{2}\sum_{\alpha\beta}\left(\frac{\partial^2 r_i}{\partial q_\alpha \partial q_\beta}\right)_0 \Delta q_\alpha \Delta a_\beta + \ldots \tag{9}$$

only the first-order derivatives enter P. For the purpose of NMA, linearization is sufficient, under the condition that the geometry of the structure is optimized.[17]

The transform of the reduced quantities to their original $3N_A$ size is well known. The Cartesian expressions for the reduced Hessian, mass matrix, and normal modes are obtained by matrix multiplications with the $m \times 3N_A$ matrix $Q = P^T(PP^T)^-$,

$$H' = Q^T H^{\mathrm{re}} Q \tag{10}$$

$$M' = Q^T M^{\mathrm{re}} Q \tag{11}$$

$$v' = P v^{\mathrm{re}}, \tag{12}$$

where the factor $(PP^T)^-$ in Q is the pseudoinverse of PP^T and accounts for any nonorthonormality of the columns of P. Calculating Q is easy in some cases, such as for VSA or MBH. However, it requires a singular value decomposition for other arbitrary reduced bases, such as the dihedral angle basis set or a SH basis set. Moreover, the identity $P^T H' P = H^{\mathrm{re}} = P^T H^{\mathrm{AA}} P$ holds (similar for M', v'), which means that the primed quantities have the original size but lie entirely within the subspace spanned by the columns of P. These equations complete the relations between the Cartesian and the reduced quantities which can be summarized as (Fig. 2a):

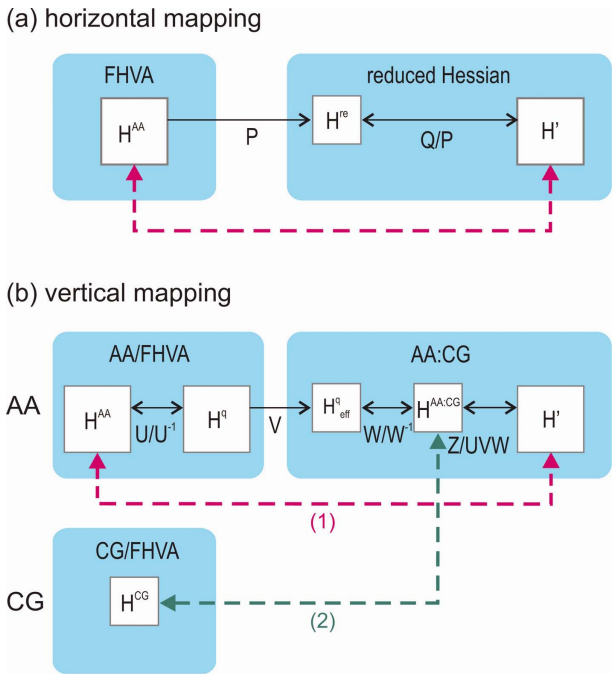

Figure 2. Horizontal and vertical mapping procedure between larger and smaller matrices. The mass matrices and displacement vectors undergo the same transformations as the Hessians. Dashed lines indicate which matrices/vectors can be compared: the dashed lines always connect matrices of equal size. a) Horizontal mapping for reduced Hessians: the back transform Q from the small Hessian H^{re} to the larger Hessian H' is well known (section Horizontal mapping for reduced basis sets). b) Vertical mapping between different scales is based on VSA and requires two steps (section Vertical mapping for coarse-grained models). First, AA/FHVA is compared with AA/VSA (H^{AA} *vs.* H'). Next, the imploded AA/VSA matrix is compared with the CG/FHVA matrix ($H^{\mathrm{AA:CG}}$ *vs.* H^{CG}). [Color figure can be viewed in the online issue, which is available at wileyonlinelibrary.com.]

$$H^{AA}, M^{AA}, v^{AA} \xrightarrow{P} H^{re}, M^{re}, v^{re} \xleftrightarrow{Q/P} H', M', v'. \quad (13)$$

Once the reduced basis set P is known, it is straightforward to transform Hessians, mass matrices, and normal modes between their original size and the projected size. It should be pointed out that the original matrices (H^{AA}, M^{AA}, v^{AA}) can never be reconstructed from their reduced counterparts (H^{re}, M^{re}, v^{re}). In a sense, (H', M', v') is the closest one can get to (H^{AA}, M^{AA}, v^{AA}) based on the information that remains in (H^{re}, M^{re}, v^{re}). Solving the NMA equations with H' and M' yields the same non-zero frequencies as solving those with H^{re} and M^{re}, except for $3N_A - m$ additional zero frequencies.

Vertical mapping for coarse-grained models

In a CG model with N_{CG} particles, the full CG Hessian has the dimension $3N_{CG} \times 3N_{CG}$ and contains the derivatives of the force field energy E^{CG} with respect to the positions r_I, $I = 1,\ldots, 3N_{CG}$, of the beads,

$$H^{CG}_{I,J} = \left(\frac{\partial^2 E^{CG}}{\partial r_I \partial r_J}\right)_0 \quad (14)$$

evaluated at the reference point r_I^0. The diagonal CG mass matrix contains the masses of the beads on the diagonal. Solving the normal mode equations

$$H^{CG}v^{CG} = (\omega^{CG})^2 M^{CG} v^{CG} \quad (15)$$

results in $3N_{CG}$ frequencies and normal mode vectors of length $3N_{CG}$.

Transforming between scales requires a mapping scheme for both the force constants and the bead masses. As an example, matrix implosion is required when comparing AA normal modes to ENM normal modes. The procedure shrinks the large AA matrices to the size of the small CG matrices. In the remainder of this section, we show how effective force constants can be adequately derived from the large Hessian using the VSA principle, followed by a redistribution of the mass of the large mass matrix. The large matrices (H^{AA}, M^{AA}) are assumed to be at the AA scale with size $3N_A$. The small matrices (H^{CG}, M^{CG}) are at the CG scale with size $3N_{CG}$. The *imploded* matrices ($H^{AA:CG}$, $M^{AA:CG}$) are labeled with AA:CG, referring to the change in size. For instance, the imploded AA Hessian $H^{AA:CG}$ is based on the AA force field but has then been imploded to the same size as the CG Hessian, which facilitates the subsequent NMA comparison.

The implosion procedure consists of three steps:

1 Express the Hessian and mass matrix in general coordinates q. Select interesting general coordinates q_s, which represent the CG coordinates.

2 Derive effective force constants and an effective kinetic tensor using VSA.

3 Redistribute the mass over the particles.

First, a subset of $3N_{CG}$ general coordinates q_s is selected that represent the CG coordinates. We restrict ourselves to CG coordinates that are linear combinations of the AA Cartesian coordinates. For instance, when using the ENM, the selected coordinates are the C_α positions. These general coordinates q_s are collected as the columns of a $3N_A \times 3N_{CG}$ matrix Q_s. The large matrices in Cartesian coordinates are transformed to the general coordinate set q (of which is q_s is a subset) as follows. The orthogonal complement Q_e of Q_s is calculated to form a complete basis set $U = [Q_s;Q_e]$, which can be achieved with a singular value decomposition of the Q_s matrix. The subscripts s and e refer to subsystem and environment, respectively, in analogy with the VSA terminology. The normal mode equations can be expressed in the new $q = \{q_s,q_e\}$ coordinates by matrix multiplication with the $3N_A \times 3N_A$ matrix U,

$$H^q = U^T H^{AA} U \quad (16)$$

$$M^q = U^T M^{AA} U. \quad (17)$$

Although M^{AA} is diagonal, the mass matrix in q coordinates might no longer be diagonal. Note that solving the equations $H^q v^q = \omega^2 M^q v^q$ would still result in the same frequencies and normal modes, when applying the back transform $v^{AA} = Uv^q$.

Second, the dimension is reduced by the VSA principle in a manner similar to dynamic model condensation in the field of finite elements. VSA dictates that the derivative of the energy with respect to the environment atoms should be zero during the vibrational analysis.[24,25] This condition forces the environment atoms to follow the motions of the subsystem atoms adiabatically.[27] Where originally Cartesian coordinates were used in the subsystem and environment definition,[24,25] here the VSA principle is applied to a subsystem consisting of the generalized q_s coordinates, which need not be Cartesian. In the case of ENM, where the q_s coordinates are the C_α positions, the VSA condition means that the C_α beads exist on an effective potential energy surface created by the environment. Simultaneously, their inertia changes to account for the inertia of the environment. This picture fits well with the concept of a CG model, which also strives to reconstruct effective potentials and masses. Additionally, it has been shown that VSA performs excellently in the low-frequency region,[27] which is the part of the spectrum that CG models are designed to reproduce. CG models poorly represent localized, higher frequency vibrations, as local details are removed. Thus VSA is well suited to construct the effective force constants from the large Hessian and an effective mass matrix from the large mass matrix.

H^q and M^q are divided into four sub-blocks corresponding to the subsystem and the environment generalized coordinates,

$$H^q = \begin{pmatrix} H^q_{ss} & H^q_{se} \\ H^q_{es} & H^q_{ee} \end{pmatrix}; \quad M^q = \begin{pmatrix} M^q_{ss} & M^q_{se} \\ M^q_{es} & M^q_{ee} \end{pmatrix}. \quad (18)$$

Applying VSA to the general subsystem/environment degrees of freedom,

$$\frac{\partial E^{AA}}{\partial q_e}(q_s, q_e) = 0 \rightarrow H^q_{es} q_s + H^q_{ee} q_e = 0 \quad (19)$$

gives the effective VSA Hessian and mass matrix in the q_s coordinates,

$$H^q_{\text{eff}} = V^T H^q V = H^q_{ss} - H^q_{se}\left(H^q_{ee}\right)^{-1} H^q_{es} \tag{20}$$

$$M^q_{\text{eff}} = V^T M^q V = M^q_{ss} + H^q_{se}\left(H^q_{ee}\right)^{-1} M^q_{ee}\left(H^q_{ee}\right)^{-1} H^q_{es} - H^q_{se}\left(H^q_{ee}\right)^{-1} M^q_{es} - M^q_{se}\left(H^q_{ee}\right)^{-1} H^q_{es} \tag{21}$$

where V is a $3N_A \times 3N_{CG}$ transformation matrix,

$$V = \left[\mathrm{I}_{3N_s}; -\left(H^q_{ee}\right)^{-1} H^q_{es}\right]^T \tag{22}$$

which projects the large matrices onto a subspace of dimension $3N_{CG}$. The corresponding normal mode equations read

$$H^q_{\text{eff}} v^q_{\text{eff}} = (\omega^q_{\text{eff}})^2 M^q_{\text{eff}} v^q_{\text{eff}}. \tag{23}$$

Previous works have addressed a similar implosion method but only for the Hessian[53,54]; we claim that the same implosion should be applied to the mass matrix as well.

Third, the discrepancy between mass matrices should be resolved. So far the effective matrices have the same size as the CG matrices. However, the kinetic tensor is given by M^{CG} for the CG model [eq. (15)], whereas it is given by M^q_{eff} for the imploded AA model [eq. (23)]. The comparison of motions using different kinetic tensors has no clear interpretation. The same kinetic tensors can be obtained by first un-mass-weighting with M^q_{eff} and re-mass-weighting with M^{CG}, using the $3N_{CG} \times 3N_{CG}$ matrix $W = (M^q_{\text{eff}})^{-1/2}(M^{CG})^{1/2}$. The resulting matrices are the AA Hessian and mass matrix imploded to the CG scale,

$$H^{\text{AA:CG}} = W^T H^q_{\text{eff}} W \tag{24}$$

$$M^{\text{AA:CG}} = W^T M^q_{\text{eff}} W \equiv M^{CG}. \tag{25}$$

The physical interpretation of this last transformation with W is that the mass in the large AA mass matrix is redistributed over the $3N_{CG}$ coordinates q_s such that it equals the mass distribution of the small CG matrix. In the ENM example, the AA masses of each residue are regrouped into an ENM bead at the C_α position, which has a mass equal to the sum of all the masses in the residue.

Ultimately, the normal mode equations make use of these imploded effective matrices

$$H^{\text{AA:CG}} v^{\text{AA:CG}} = (\omega^{\text{AA:CG}})^2 M^{\text{AA:CG}} v^{\text{AA:CG}}, \tag{26}$$

which give $3N_{CG}$ frequencies and $3N_{CG}$ normal modes of length $3N_{CG}$ with the correct kinetic tensor, allowing for direct comparison to the CG quantities. The back transform of the imploded quantities to their original size starts with a transform W^{-1} to undo the mass redistribution. This is followed by a transform $V^T(VV^T)^-$ from the subset of coordinates to all of the q coordinates, where $(VV^T)^-$ is the pseudoinverse of VV^T. Finally, a transform U^{-1} to the Cartesian coordinates is applied using the $3N_{CG} \times 3N_A$ matrix $Z = W^{-1}V^T(VV^T)^- U^{-1}$.

$$H' = Z^T H^{\text{AA:CG}} Z \tag{27}$$

$$M' = Z^T H^{\text{AA:CG}} Z \tag{28}$$

$$v' = UVW v^{\text{AA:CG}}. \tag{29}$$

The identity $(UVW)^T H' (UVW) = H^{\text{AA:CG}} = (UVW)^T H^{\text{AA}}(UVW)$ holds (similar for M', v'), which means that the primed quantities have the original size but lie entirely within the subspace spanned by the q_s coordinates. The relations between the large and imploded Hessians are summarized by (Fig. 2b)

$$H^{\text{AA}}, M^{\text{AA}}, v^{\text{AA}} \overset{U/U^{-1}}{\leftrightarrow} H^q, M^q, v^q \overset{V}{\rightarrow} H^q_{\text{eff}}, M^q_{\text{eff}}, v^q_{\text{eff}} \tag{30}$$

$$\overset{W/W^{-1}}{\leftrightarrow} H^{\text{AA:CG}}, M^{\text{AA:CG}}, v^{\text{AA:CG}} \overset{Z/UVW}{\leftrightarrow} H', M', v'. \tag{31}$$

Fortunately, the last mass-redistributing step does not have to be executed explicitly, as one can show that the mass-weighted VSA normal modes are equal to the mass-weighted imploded normal modes,

$$\tilde{v}^q_{\text{eff}} = (M^q_{\text{eff}})^{1/2} v^q_{\text{eff}} = (M^{\text{AA:CG}})^{1/2} v^{\text{AA:CG}} = \tilde{v}^{\text{AA:CG}}. \tag{32}$$

In practice, one selects the $3N_{CG}$ coordinates q_s, applies VSA, and uses the mass-weighted VSA normal modes directly for comparison with the CG model. The overlap between the CG vectors v^{CG} and imploded AA vectors $v^{\text{AA:CG}}$ is calculated using their kinetic tensor M^{CG},

$$(v^{CG})^T M^{CG} v^{\text{AA:CG}} = (\tilde{v}^{CG})^T \tilde{v}^{\text{AA:CG}} = (\tilde{v}^{CG})^T \tilde{v}^q_{\text{eff}}. \tag{33}$$

The vertical mapping described above allows us to outline a standard procedure for comparing AA and CG scales (Fig. 2b). The procedure contains two parts:

1 Compare the FHVA modes at the AA scale (AA/FHVA) with the imploded Hessian using VSA (AA/VSA), where the subsystem coordinates in the VSA are the generalized CG coordinates. If they compare well, the generalized coordinates in the imploded Hessian (AA/VSA) are adequate variables that retain the essential dynamics of the AA model.

2 Compare the FHVA modes at the CG scale (CG/FHVA) with the imploded AA/VSA modes. If they compare well, the CG force field parameters adequately describe the force constants of the AA force field.

Test Cases: Alpha Helix and Globular Protein

To demonstrate the comparison of normal modes at different scales, we use a simple alpha helix with 31 residues and $N_A = 552$ atoms, as can be seen in Figure 3a. The starting structure is an alpha helix monomer taken from X-ray diffraction data in the Protein Database (PDB code: 1GCL).[55] The geometry of the helix is optimized using CHARMM [56] in conjunction with the CHARMM22 force field with the CMAP backbone correction.[57] The optimized structure is then used as an input for all subsequent vibrational calculations and as an input to build all CG models. The NMA is performed with functions of the VIBRAN module of CHARMM, using the DIAG (for FHVA),[28–30] VSA,[24,25] and MBH[18] commands. The CHARMMing interface (www.charmming.org) is used extensively for

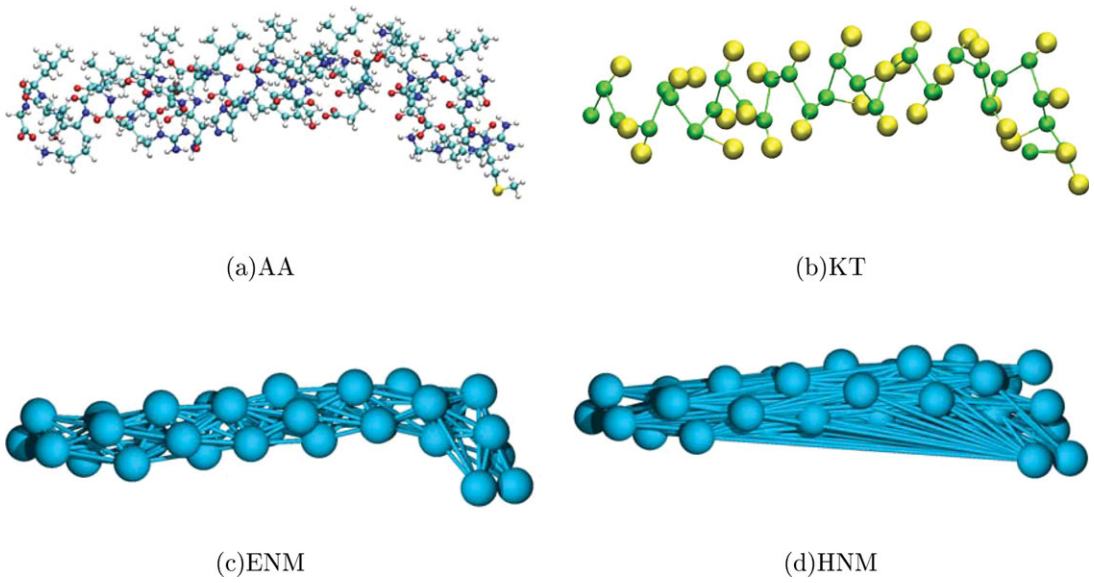

Figure 3. The alpha helix is represented at multiple scales: a) AA with 552 atoms, b) KT with 61 beads, that is, two beads per residue or one for glycine, c) ENM with 31 beads, with springs between C_α pairs within a cutoff radius of 10 Å, d) HNM, as for ENM, but with unreasonable springs connecting C_α pairs that are far apart.

structure preparation and to generate CHARMM input scripts for geometry optimization.[58] Scripts and other relevant simulation details are provided in Supporting Information.

The horizontal reduced Hessian techniques used in this article are the (1) FHVA, (2) VSA, (3) MBH, and (4) SH. The standard FHVA results in 1656 frequencies in the AA case. Three subsystem choices are considered for the VSA, including all of the C_α atoms, only the C_α atoms of the even numbered residues, or only the C_α atoms of the odd numbered residues.[27] For the MBH, blocks are chosen as in the typical RTB method, where each block consists of one amino acid including the amide bond and the side chain.[21,22] We also evaluated the MBH using two amino acids per block, for both the AA scale and KT scale (see below). These methods are available in TAMkin, a free post-processing toolkit for NMA and kinetics.[59] The basis set of the SH method contains 78 spherical harmonics and is discussed in section Projection on SH as a separate metric for mode comparison. The comparison of FHVA *versus* VSA, MBH, and SH based on horizontal mapping has been done previously at the AA scale[27,60]; therefore, the focus of this article is upon the vertical mapping between various CG scales.

The first CG protein model (KT) used in this article is a Gō-like model[50] based off of previous work by Thirumalai and coworkers.[39,51,52] The assumption underlying all Gō-like models is that below a protein's melting temperature T_m, the native state is the global free energy minimum.[50] Therefore, native contacts are more stable than non-native contacts and are assigned an attractive potential, whereas non-native contacts are destabilizing and are assigned a repulsive potential. In the KT model, two interaction sites are used per residue (except for glycine): the backbone particle, derived from the C_α position, and the side-chain particle, derived from the AA side-chain center of mass (Fig. 3b). The strengths of the native contact interactions are statistically derived from experimental residue–residue pairwise interactions.[61] This contact matrix is then scaled by an empirical prefactor (parameter nscale) to produce a physiological T_m. Further simulation details may be found in the Supporting Information.

The second CG model used is the ENM. This model puts a bead at each C_α position and assigns it a mass equal to that of the original residue (Fig. 3c).[43] Neighboring C_α pairs are connected by springs with a force constant $k_1 = 60$ kcal mol^{-1} Å^{-2}. Other C_α pairs that lie within a cutoff distance of $r_c = 10$ Å are coupled with a force constant $k_2 = 6$ kcal mol^{-1} Å^{-2}. Beyond the cutoff, there is no coupling ($k_3 = 0$). These force constant values were shown to provide good agreement with the AA frequencies.[62]

Additionally, a CG model has been invented with intentionally unreasonable force constants. This nonsense model is expected to perform badly when compared with the AA results and allows us to test whether a metric can detect poor performance. This HNM is the same as the ENM, except $k_1 = 0$, $k_2 = 0$, and $k_3 = 20$ kcal mol^{-1} Å^{-2}. C_α pairs beyond a cutoff radius of 10 Å are connected by springs, whereas nearby C_α pairs are not coupled (Fig. 3d).

The alpha helix is used to investigate a series of metrics that can evaluate the quality of CG models in section Metrics. In section Illustration with a Globular Protein, the developed tools are applied to a real globular protein. The protein G-related albumin-binding (GA) module demonstrates a high binding affinity for human serum albumin. The GA module is found in multiple surface proteins of the *Streptococcus* bacterial family. This domain is one of the earliest examples of module shuffling and is thought to play a crucial role in the evolutionary fitness of the bacteria that express it.[63] Our model of the GA module is based upon a ^{1}H NMR solution structure taken from the poly(A)-binding protein of the *Peptostreptococcus magnus* bacteria (PDB code: 1PRB, residues 7–53). [64] The

structure is composed of a three-helix bundle packed together in an antiparallel fashion and consists of 47 residues and $N_A = 746$ atoms. Because of its small size and simple topology, 1PRB is an ideal test system for both experimental (probing the kinetics and establishing the ultrafast folding limit[65]) and theoretical (modeling folding as diffusion along a 1D reaction coordinate[66]) biophysical studies. Furthermore, previous studies have established the efficacy of applying a variety CG models to the GA domain. Both Gō-like[66] and transferable[67] CG models have been successfully used to study various aspects of this domain, allowing our novel analysis techniques to be evaluated on their own merits.

The same four CG models are used for 1PRB as for the alpha helix: AA with the CHARMM22 force field, KT with a statistical pairwise potential and *ad hoc* nscale parameter (see Supporting Information), ENM, and HNM. A subtle difference between the CG models of the two systems is that the CG alpha helix has been constructed from optimized AA coordinates, whereas the CG 1PRB system has been generated directly from the experimental structure. Before applying NMA, the structures at each scale are reoriented to align their principal axes of inertia.

Metrics

The most basic NMA results to be compared are frequencies and normal modes. Derived quantities include: thermal fluctuations, probability similarity, Hessian similarity, collectivity of modes, shape derivatives, projection on SH, elastic modulus, difference in vibrational free energy, and heat capacity. Five of these metrics are truly dimension-independent: shape derivatives, SH analysis, elastic modulus, difference in vibrational free energy, and heat capacity. Other metrics can only be calculated after a horizontal or vertical mapping is applied first. It is important to correctly mass-weight the reduced and imploded Hessians in these analyses, otherwise the results will not be valid.

Frequencies

The following two types of plots are useful to visualize the difference in trend between the frequencies $\omega_i^{\mathbf{1}}$, $i = 1,\ldots,n_{\mathbf{1}}$, and $\omega_i^{\mathbf{2}}$, $i = 1,\ldots,n_{\mathbf{2}}$, of two different arbitrary scales **1** and **2**.

- Plot the frequencies $\omega_i^{\mathbf{1}}$ and $\omega_i^{\mathbf{2}}$ *versus* their mode number i on the same plot, or plot the frequencies $\omega_i^{\mathbf{1}}$ *versus* the frequencies $\omega_i^{\mathbf{2}}$. When $n_{\mathbf{1}}$ and $n_{\mathbf{2}}$ differ, only plot the lowest common frequencies.
- Plot the density of states profile for each method on the same plot.

The first type of plot visualizes the deviations between frequencies. When the frequencies of scale **2** overestimate those of scale **1**, it means that the model in scale **2** is more rigid than in scale **1**. By fitting a line, this misestimation is quantified by a proportionality factor f,

$$\omega_i^{\mathbf{2}} = f\,\omega_i^{\mathbf{1}}. \tag{34}$$

Another effect can cause overestimation: some modes might be missing at a coarser scale. Indexing the modes by increasing frequency does not ensure that the modes have similar character. One should complement the comparison of frequencies with the comparison of normal mode vectors (see section Normal modes) before drawing conclusions.

The density of states profile is estimated by summing Gaussians with a chosen width σ that are centered around the frequencies ω_i,

$$g(\omega) = \frac{1}{n}\sum_{i=1}^{n}\frac{1}{\sqrt{2\pi\sigma}}\exp\left(-\frac{(\omega-\omega_i)^2}{2\sigma}\right). \tag{35}$$

Division by n ensures that the area under the profile is normalized at each scale. The density of states profile allows one to visually detect which frequency regions broaden, narrow, or shift.

For the alpha helix system, we compared the FHVA frequencies of the AA, KT, ENM, and HNM scales in Figure 4. In the low frequency region, below 50 cm^{-1}, the KT model underestimates the AA frequencies ($f = 0.61$) and the ENM reproduces them well ($f = 1.13$). The HNM makes a large unphysical jump at 54 cm^{-1}. A linear fit below 50 cm^{-1} gives $\omega^{HNM} = 0.61\ \omega^{AA} + 6.01$ (in cm^{-1}), demonstrating the shift of the HNM

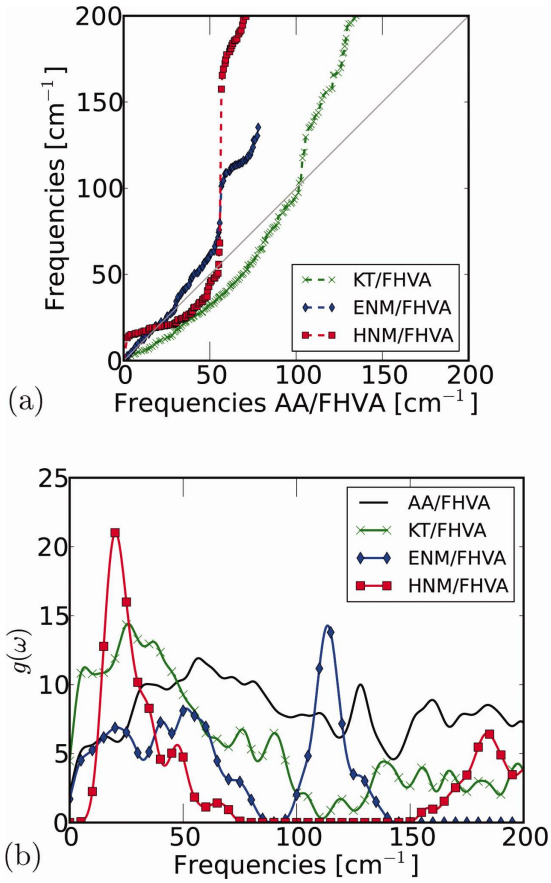

Figure 4. Alpha helix—frequencies in cm^{-1} calculated with the full Hessian (FHVA) at the AA, KT, ENM, and HNM scale. a) Frequencies of CG scales *versus* AA scale. b) Density of states $g(\omega)$ as in eq. (35). [Color figure can be viewed in the online issue, which is available at wileyonlinelibrary.com.]

frequencies with respect to AA. This means that, for the collective motions, the KT model is too flexible, the ENM has the correct flexibility, and the HNM is useless for frequency reproduction.

Normal modes

The normal mode vectors v_i, $i = 1,\ldots,n$ are labeled by their frequency ω_i and are orthogonal with respect to the mass matrix M,

$$v_i^T M v_j = \delta_{ij} = \tilde{v}_i^T \tilde{v}_j. \tag{36}$$

A cumbersome and imprecise way of comparing the modes $v_i^{\mathbf{1}}$, $i = 1,\ldots,n_{\mathbf{1}}$, and $v_i^{\mathbf{2}}$, $i = 1,\ldots,n_{\mathbf{2}}$ at two different scales **1** and **2** is by visualizing a movie of the vibration of each normal mode. A quantitative comparison is obtained using the overlap between modes of equal length. If the lengths differ, horizontal mapping or vertical mapping is first applied. The square overlap between two modes is defined as the square of the dot product between the normalized mass-weighted normal mode vectors,

$$O_{ij} = O(\omega_i^{\mathbf{1}}, \omega_j^{\mathbf{2}}) = \left|\left\langle \omega_i^{\mathbf{1}} | \omega_j^{\mathbf{2}} \right\rangle\right|^2 = \left|\tilde{v}_i^{\mathbf{1}T} \tilde{v}_j^{\mathbf{2}}\right|^2. \tag{37}$$

The square overlap is a value between zero and one, where larger values indicate high similarity between the modes.

This definition of the square overlap only makes sense when the kinetic tensor is the same for models **1** and **2**. In the horizontal mapping scheme (Fig. 2), the AA/FHVA mass matrix M [eq. (2)] is not identical to the reduced mass matrix transformed back to its original size M' [eq. (12)], but the difference lies entirely in the motions that are projected out. Reduced mode vectors v' can be mass-weighted with either M or M': the resulting mass-weighed vectors $\tilde{v}'$ are the same. Therefore, the mass matrix to use in the horizontal mapping is the M matrix for AA/FHVA and the M' matrix for the reduced techniques. Then the overlap is calculated correctly as the dot product of $\tilde{v}$ and $\tilde{v}'$.

In the vertical mapping, the implosion procedure (section Vertical mapping for coarse-grained models) ensures that $M^{\mathrm{AA:CG}}$ is equal to M^{CG}. Therefore, the imploded mode vectors $v^{\mathrm{AA:CG}}$ and the CG mode vectors v^{CG} should be both mass-weighted with the same matrix M^{CG} to obtain the mass-weighed vectors $\tilde{v}^{\mathrm{AA:CG}}$ and $\tilde{v}^{\mathrm{CG}}$. We established that the mass-weighted imploded vector $\tilde{v}^{\mathrm{AA:CG}}$ is equal to the vector that results directly from the VSA diagonalization, $\tilde{v}^q_{\mathrm{eff}}$, so in practice, the overlap is correctly calculated as the dot product of $\tilde{v}^q_{\mathrm{eff}}$ and $\tilde{v}^{\mathrm{CG}}$ [eq. (33)].

Another comparison method is the cumulative square overlap. The k-cumulative square overlap to mode $v_i^{\mathbf{1}}$ is defined as the sum of the highest k square overlaps with the scale **2** modes,

$$P_i^{(k)} = \sum_j^k O(\omega_i^{\mathbf{1}}, \omega_j^{\mathbf{2}}). \tag{38}$$

The total cumulative square overlap to mode $v_i^{\mathbf{1}}$ is then defined as the sum of all square overlaps between the mode and each of the scale **2** modes,

$$P_i = \sum_{j=1}^{n_{\mathbf{2}}} O(\omega_i^{\mathbf{1}}, \omega_j^{\mathbf{2}}) \tag{39}$$

When neither of the normal mode sets is overcomplete, the cumulative square overlap lies between zero and one. A high value indicates that a mode i of scale **1** is well represented by the set of scale **2** modes.

The square overlap and cumulative square overlap are conveniently represented by the following plots:

- Plot the square overlap $O(\omega_i^{\mathbf{1}}, \omega_j^{\mathbf{2}})$ with color-coding. Dark color refers to high overlap and light color refers to low overlap, where the x and y axes are the corresponding frequencies $\omega_i^{\mathbf{1}}$ and $\omega_j^{\mathbf{2}}$.
- Plot the cumulative square overlap P_i (and/or $P_i^{(k)}$) *versus* the mode number i, or *versus* the corresponding frequency $\omega_i^{\mathbf{1}}$.

A dark dot at position (i,j) in plot A indicates that the motion of mode i at scale **1** is well reproduced by mode j of scale **2**. The location of the dot indicates whether the frequency of the mode is well reproduced; dots close to the diagonal indicate similar frequencies between the two scales. The plot also indicates which frequencies ω_i are not reproduced at all and the general trend (overestimation or underestimation). In large molecular systems, the near-degeneracy of the frequencies makes the one-to-one comparison of the modes less useful. Plot A would show a blur of medium colored overlaps because of mode mixing. The cumulative square overlap averages out over the degenerate modes, so plot B should be used to complement plot A to eliminate the effects of degeneracy.

We have used the overlap plots to compare the modes and frequencies of the AA, KT, ENM, and HNM scales after vertical mapping. The AA/VSA implosion technique, where the subsystem contains 31 C_α positions, reduces the mode vectors to the correct size, as can be verified in Table 1. First, AA/FHVA is compared to imploded AA/VSA to verify whether the implosion technique at the AA scale is a valid approximation. Figure 5a confirms the validity in the low frequency regime. The (cumulative) square overlap plot of KT/FHVA and KT/VSA also shows a strong similarity (Supporting Information Figs. S.I.2 and S.I.3). Second, the AA/VSA is compared with the KT/VSA, ENM/FHVA, and HNM/FHVA in Figures 5b–5d. These illustrate

Table 1. Alpha helix—number of atoms/beads at each scale and number of frequencies using different reduced Hessian techniques at the different scales.

	Particles	FHVA	VSA	VSA$^{\mathrm{odd}}$	VSA$^{\mathrm{even}}$	MBH$_1$	MBH$_2$	SH
AA	552	1656	93	48	45	186	90	78
KT	61	183	93	48	45	–	90	78
ENM	31	93	93	48	45	–	–	78
HNM	31	93	93	48	45	–	–	78

Note that VSA is identical to FHVA for ENM and HNM. VSA results in the same dimension (93) for each scale and is used for vertical implosion.

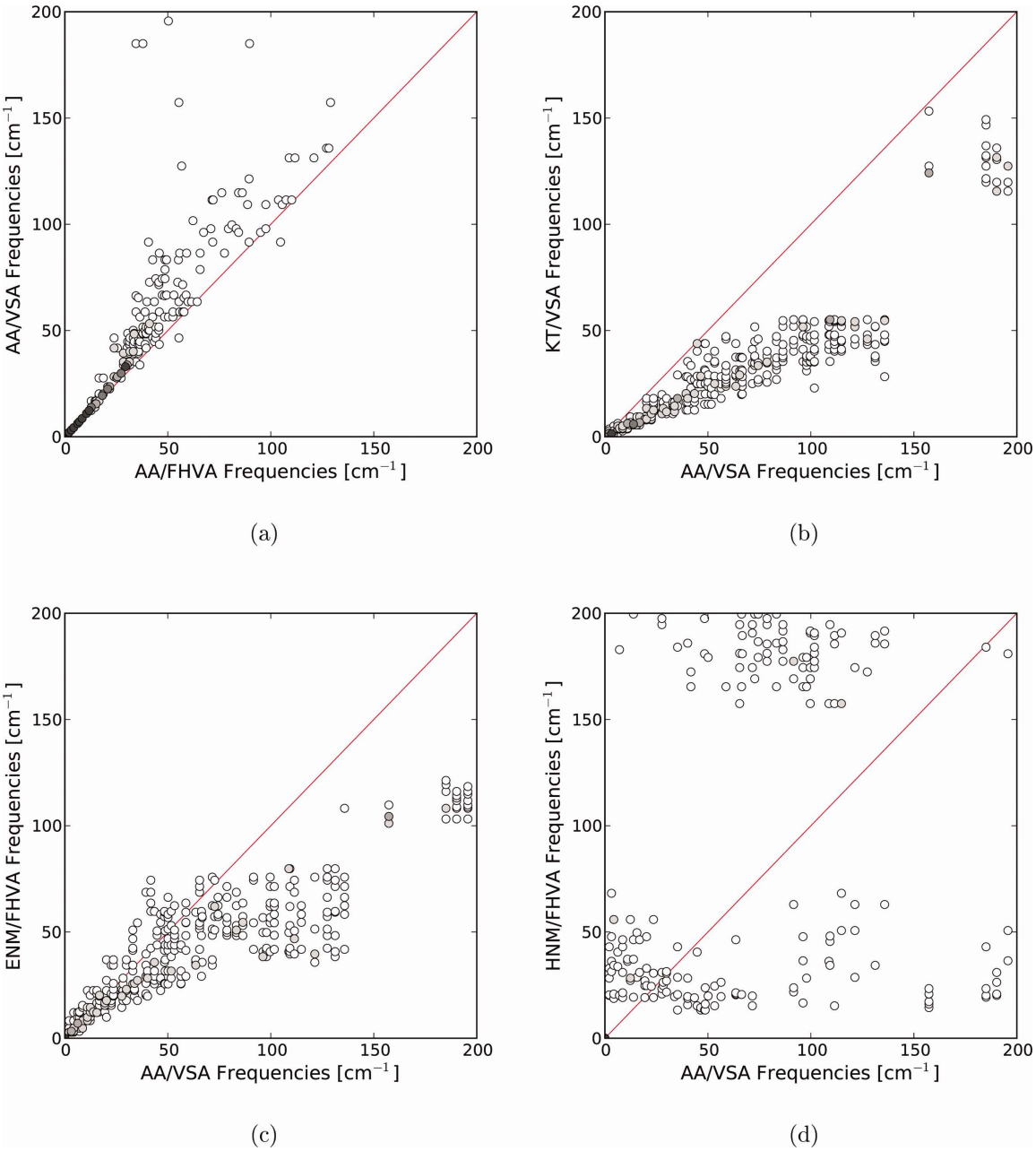

Figure 5. Alpha helix—direct comparison of modes and frequencies of the KT, ENM, and HNM scales with the AA scale. a) First, AA/FHVA is compared to AA/VSA to verify that the VSA has high overlaps in the low frequency region. See Supporting Information for KT/FHVA *versus* KT/VSA. b–d) Second, the imploded vectors are compared with the CG vectors: b) AA/VSA *versus* KT/FHVA, c) AA/VSA *versus* ENM/VSA, d) AA/VSA *versus* HNM/FHVA. Darker dots represent higher squared overlaps; values below 0.05 are not printed. [Color figure can be viewed in the online issue, which is available at wileyonlinelibrary.com.]

that the ENM has reasonable mode and frequency reproduction, that the KT model is red shifted, and that the HNM produces nonsensical results, as expected. The cumulative square overlap plots are superfluous for the vertical comparison across scales. Because all imploded Hessians have an equal rank, all cumulative square overlaps become unity.

We performed a horizontal mapping between the FHVA, VSA, MBH, and SH reduced Hessian techniques on the AA scale (Supporting Information Figs. S.I.4–S.I.14). Both the square overlap plots and the cumulative square overlap plots are useful, as projection makes the rank of the matrices unequal. VSA shows remarkably high overlaps in the low frequency region, a result consistent with other investigations.[27] MBH also performs well while the cumulative square overlap values of SH decrease sharply beyond the low frequency (<25 cm^{-1}) region.

Thermal fluctuations

Atoms are nonstationary and vibrate around their reference positions r due to temperature. These thermal fluctuations Δr are experimentally observable with X-ray crystallography (B-

factors) and NMR measurements. In the harmonic approximation, the average fluctuations are readily calculated from normal modes and frequencies. For classical harmonic vibrations, the Boltzmann factor is proportional to

$$P(\Delta r) \propto \exp\left(-\frac{\Delta r^T H \Delta r}{2k_B T}\right) \quad (40)$$

with k_B the Boltzmann constant, T the absolute temperature, and H the Hessian in Cartesian coordinates. This is a multivariate normal distribution, where the average fluctuations in a constant temperature ensemble are calculated as a sum running over the non-zero frequencies,

$$\langle \Delta x_A^2 \rangle = k_B T \sum_{i=1}^{n} \frac{|\tilde{v}_{i,Ax}|^2}{m_A \omega_i^2} \quad (41)$$

for each particle, $A = 1,\ldots,N_A$ with mass m_A (similar for Δy_A and Δz_A). The vector $\tilde{v}_i$ is the normalized, mass-weighted ith normal mode corresponding to frequency ω_i and $\tilde{v}_{i,Ax}$ is its Ax component. The total fluctuation of the particle becomes

$$\langle \Delta r_A^2 \rangle = k_B T \sum_{i=1}^{n} \frac{|\tilde{v}_{i,Ax}|^2 + |\tilde{v}_{i,Ay}|^2 + |\tilde{v}_{i,Az}|^2}{m_A \omega_i^2}. \quad (42)$$

Similar expressions hold for the reduced models and the various CG models.

At thermal equilibrium, the energy is equally distributed over the different degrees of freedom. The same amount of energy, $k_B T$, populates each mode, bringing the total energy of a system with n vibrations to $E_{tot} = nk_B T$. The amplitude of a vibrational motion with frequency ω_i is given by $\sqrt{k_B T}/\omega_i$. Collectively, the total amount of fluctuation of the normal coordinates Q_i is given as:

$$k_B T \mathcal{N}_{mw} = \sum_{i=1}^{n} \langle Q_i^2 \rangle = k_B T \sum_{i=1}^{n} \frac{1}{\omega_i^2}. \quad (43)$$

The number $\mathcal{N}_{mw}$ is a measure of the molecule's overall flexibility, as it equals the total amount of thermal fluctuations of the mass-weighted Cartesian coordinates per $k_B T$:

$$k_B T \mathcal{N}_{mw} = \sum_A m_A \langle \Delta r_A^2 \rangle = k_B T \sum_{i=1}^{n} \sum_{A,\mu=x,y,z} m_A \frac{|\tilde{v}_{i,A\mu}|^2}{m_A \omega_i^2} = k_B T \mathrm{tr}(\tilde{H}^-), \quad (44)$$

where $\mathrm{tr}(\tilde{H}^-)$ is the trace of the pseudoinverse of the mass-weighted Hessian. A CG model has fewer frequencies than the AA model and has a lower energy E_{tot} in thermal equilibrium. The largest contributions to the fluctuations come from low frequency modes. Despite the lower energy, a CG model may still be capable of reproducing the fluctuation profile, provided it accurately describes the low frequency spectrum. The difference in overall flexibility is well quantified by the ratio $\mathcal{N}_{mw}^{\mathbf{1}}/\mathcal{N}_{mw}^{\mathbf{2}}$ between two models **1** and **2**.

The fluctuations may be plotted against the atom or residue number. A profile peak corresponds to a region of high flexibility, referred to as a hot spot. Conversely, low profile values correspond to relatively immobile areas of the molecular system.[68] Two issues are encountered when comparing different scales **1** and **2**: the differing number of fluctuations to be plotted (x-axis) and the normalization of fluctuation profiles (y-axis). The first issue is solved by plotting the thermal fluctuations of a subset of the atoms or using horizontal or vertical mapping (see sections Horizontal mapping for reduced basis sets and Vertical mapping for coarse-grained models). The second issue requires profile normalization. The difference in number of particles and particle masses between scales can cause deviation in the range of the profiles. Normalization with respect to the highest peak in each profile is possible, or alternatively, normalization by the total amount of fluctuations (not mass-weighted), $k_B T \mathcal{N}$,

$$k_B T \mathcal{N} = \sum_A \langle \Delta r_A^2 \rangle = k_B T \sum_{i=1}^{m} \sum_{A,\mu=x,y,z} \frac{|\tilde{v}_{i,A\mu}|^2}{m_A \omega_i^2} = k_B T \mathrm{tr}(H^-), \quad (45)$$

where $\mathrm{tr}(H^-)$ is the trace of the pseudoinverse of the Hessian. For CG models, the sum in $\mathcal{N}^{CG}$ runs over the CG particles using the CG masses. For imploded models, $\mathcal{N}^{AA:CG}$ equals the trace of the imploded Hessian ($H^{AA:CG}$), or the sum can be calculated using the CG masses (as $M^{AA:CG} = M^{CG}$) and the imploded mass-weighted vectors ($\tilde{v}^{AA:CG}$). As in the mass-weighted case, the ratio $\mathcal{N}^{\mathbf{1}}/\mathcal{N}^{\mathbf{2}}$ can also highlight differences in overall protein flexibility. In addition, the difference in the fluctuation profiles can be quantified with ρ, the correlation coefficient between the two graphical curves.

More generally, the matrix

$$\langle \Delta r_{A\mu} \Delta r_{B\nu} \rangle = k_B T \sum_{i,j=1}^{m} \frac{\tilde{v}_{i,A\mu} \tilde{v}_{j,B\nu}}{\sqrt{m_A m_B}\, \omega_i \omega_j} \quad (46)$$

describes the correlation between the fluctuation of the Cartesian coordinates $A\mu$ and $B\nu$. High correlation values for a set of atoms indicate that their motions are highly coupled. Inspection of the correlation matrix can reveal coherent domain motions and couplings.

Figure 6 and Table 2 investigate the thermal fluctuations of the helix at the AA, KT, ENM, and HNM scales. The plots of AA/FHVA *versus* AA/VSA and KT/FHVA *versus* KT/VSA lie virtually on top of each other (Supporting Information Fig. S.I.15), justifying the implosion technique. According to the values of $\mathcal{N}_{mw}$ (and $\mathcal{N}$) in Table 2, the implosion with VSA masks only 8% (11%) of the fluctuations in the AA model and 4% (4%) in the KT model with respect to FHVA. Although our mapping approach is more rigorous, the intuitive technique of only plotting the C_α fluctuations gives similar profiles (Supporting Information Figs. S.I.16 and S.I.17). Table 2 further compares the overall flexibility using the summation of frequencies in eq. (43) for $\mathcal{N}_{mw}$ and the imploded vectors in eq. (45) for $\mathcal{N}$. ENM is slightly more rigid than AA, whereas KT is too flexible. Consequently, the difference in flexibility, $\mathcal{N}_{mw}^{KT}/\mathcal{N}_{mw}^{AA} = 2.72$, could be resolved by rescaling all the force constants of the KT model accordingly. The difference in overall flexibility is also illustrated by the non-normalized fluctuation profiles (Fig. 6a). HNM is very rigid in comparison.

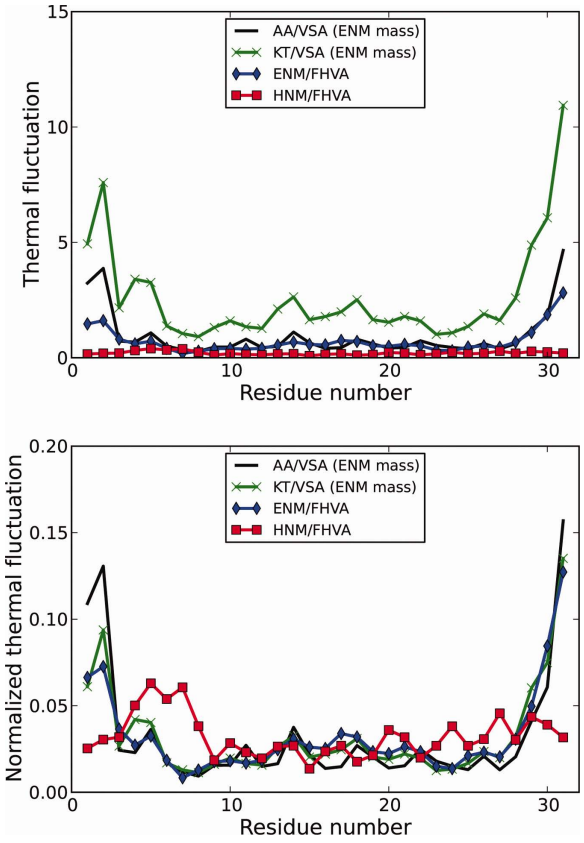

Figure 6. Alpha helix—thermal fluctuations $\langle \Delta r_I^2 \rangle$ at 300 K as a function of the residue number at different scales. a) Thermal fluctuation profile in Å^2. The imploded vectors are used in eq. (42) for AA and KT. b) Normalized fluctuation profile via division by $k_B T \mathcal{N}$ [eq. (45)]. [Color figure can be viewed in the online issue, which is available at wileyonlinelibrary.com.]

The normalized fluctuation profiles after implosion (Fig. 6b) are obtained via division by $k_B T \mathcal{N}$ and highlight the regions of relatively high and low protein flexibility. The hot spots and immobile regions of the AA scale are reproduced well by the KT and ENM scales, with correlation coefficients of 0.934 and 0.911, respectively (Table 2). Even with KT being too flexible, the model nevertheless reproduces the correct relative flexibility. The good ENM results are not surprising, as the ENM force constants used in this article were specifically designed to reproduce the lowest frequency.[62] In contrast, the HNM has no flexible ending points as in the AA scale and has a correlation coefficient of −0.030. The thermal fluctuation profiles, their normalization constants, and their correlation coefficients are adequate measures to evaluate the flexibility of a protein model as they discriminate unreasonable models.

Probability similarity

It is possible to compare the probability distributions themselves rather than the thermal average of the displacements. The overlap of the distributions may be measured by the normalized cross-correlation C of the probability densities $P^{\mathbf{1}}$ and $P^{\mathbf{2}}$ of the mass-weighted displacements $\Delta\tilde{r} = M^{1/2}\,\Delta r$ corresponding with two scales **1** and **2**,

$$C(\mathbf{1},\mathbf{2}) = \frac{J_{\mathbf{1},\mathbf{2}}}{\sqrt{J_{\mathbf{1},\mathbf{1}} J_{\mathbf{2},\mathbf{2}}}}, \tag{47}$$

where J is an overlap integral,

$$J_{\mathbf{1},\mathbf{2}} = \int \left(P^{\mathbf{1}}(\Delta\tilde{r}) P^{\mathbf{2}}(\Delta\tilde{r})\right)^k d\Delta\tilde{r}, \tag{48}$$

with k an arbitrary positive power. For $k = 1$, C is known as the Carbo similarity coefficient to measure the overlap of quantum chemical electron densities.[69]

In the classical limit, the displacements follow a multivariate Gaussian distribution [eq. (40)], and the correlation may be expressed as a product of pseudodeterminants of the correlation matrices,[70] which are here given by the pseudoinverses of the mass-weighted imploded Hessians $\tilde{H}^{\mathrm{AA:CG}}$,

$$C(\mathbf{1},\mathbf{2}) = 2^{n/2} \sqrt[4]{\frac{\det^* \tilde{H}^{\mathbf{1}} \det^* \tilde{H}^{\mathbf{2}}}{\det^{*2}(\tilde{H}^{\mathbf{1}} + \tilde{H}^{\mathbf{2}})}}. \tag{49}$$

Here, n is the number of non-zero frequencies (assumed to be equal for the imploded Hessians), and det* is the pseudodeterminant of a matrix, calculated as the product of the non-zero eigenvalues of the matrix. In terms of the frequencies $\omega_i^{\mathbf{1}+\mathbf{2}}$ of the sum $\tilde{H}^{\mathbf{1}} + \tilde{H}^{\mathbf{2}}$, the expression reads

$$C(\mathbf{1},\mathbf{2}) = 2^{n/2} \prod_{i=1}^{n} \frac{\sqrt{\omega_i^{\mathbf{1}} \omega_i^{\mathbf{2}}}}{\omega_i^{\mathbf{1}+\mathbf{2}}}. \tag{50}$$

Table 2. Alpha helix—measuring the overall flexibility of the helix using (1) $\mathcal{N}_{\mathrm{mw}}$, the total amount of mass-weighted thermal fluctuations per $k_B T$, defined in eq. (43), in Å^2 amu mol kcal^{-1}, (2) N, the total amount of thermal fluctuations per $k_B T$, defined in eq. (45), in Å^2 mol kcal^{-1}, and (3) $\rho(1,2)$, the correlation coefficient between the fluctuation profiles of two scales 1 and 2.

$\mathcal{N}_{\mathrm{mw}}$	Implosion	$\mathcal{N}_{\mathrm{mw}}$	Scale comparison
AA/FHVA	6369.0	AA	5861.4
AA/VSA	5861.4	KT	15932.1
KT/FHVA	16590.3	ENM	4389.0
KT/VSA	15930.1	HNM	1269.1
$\mathcal{N}$	Implosion	$\mathcal{N}$	Scale comparison
AA/FHVA	1058.9	AA	49.7
AA/VSA	938.2	KT	135.8
KT/FHVA	254.1	ENM	37.1
KT/VSA	244.7	HNM	10.6

ρ(1,2)	AA	KT	ENM	HNM
AA	1.000	0.934	0.911	−0.030
KT		1.000	0.970	0.086
ENM			1.000	−0.013
HNM				1.000

For $\mathcal{N}_{\mathrm{mw}}$ and $\mathcal{N}$, the validity of the implosion is first verified by comparing FHVA and VSA (column 'implosion') and next scales are compared using the imploded AA:CG vectors (column 'scale comparison'). For $\rho(\mathbf{1},\mathbf{2})$, the imploded fluctuation profiles (AA/VSA, KT/VSA) are used.

Interestingly, the expression is independent of the power k and temperature. The cross-correlation lies between zero and one, where the maximum corresponds with a perfect overlap of the distributions, including the directions and the amplitudes of the vibrations.

A problem with the metric C is the dependence on the pseudodeterminants, which makes C overly sensitive to errors when the system size n increases. For instance, assume that scale **2** is too flexible with respect to scale **1**, such that all the frequencies of scale **1** overestimate all the frequencies of scale **2** by the same factor $f > 1$. Also assume that the eigenvectors of the two scales are perfectly aligned. Using the relation $\omega_i^{\mathbf{2}} = f\,\omega_i^{\mathbf{1}}$ in eq. (50), the cross-correlation becomes $C(\mathbf{1}, \mathbf{2}) = (2f/(1 + f^2))^{n/2}$. For a system size of $n = 100$ frequencies and an overestimation $f = 2$, the cross-correlation has already decreased to $C \approx 10^{-5}$, and it would decrease further if the eigenvectors were not perfectly aligned. This over-sensitivity results in low C values for larger systems, and it is recommended to compare the logarithm of C. Another problem is that C is sensitive to errors over the whole frequency range. To validate a CG model, a metric is ideally more focused on the lower spectrum. As all frequencies equally contribute in eq. (50), C is expected to poorly recognize the CG models that have a good reproduction of the low energy modes in the spectrum.

The cross-correlation compares the complete joint probability distributions of two scales. Another approach is comparing the probability on a per particle basis, by averaging the cross-correlation between the distributions of each individual particle at the two scales. Such an approach was successfully applied by Riccardi et al. to investigate the effects of a protein crystal environment on the anisotropic displacements.[71] The cross-correlation $C_A(\mathbf{1}, \mathbf{2})$ between two scales of a particle A is calculated using the 3×3 sub-blocks $\tilde{H}^{\mathbf{1}}_{A,A}$ and $\tilde{H}^{\mathbf{2}}_{A,A}$ of the mass-weighted imploded Hessians in eq. (49). The particle-averaged cross-correlation is then calculated as:

$$C_{\text{ave}}(\mathbf{1}, \mathbf{2}) = \frac{1}{N_A} \sum_A C_A(\mathbf{1}, \mathbf{2}). \tag{51}$$

The metric C_{ave} has the advantage that, especially for larger systems, its value is less sensitive than C, because each of the C_A contributions is the cross-correlation of 3 degrees of freedom (the displacements of a single atom). For instance, in the hypothetical case mentioned above with $f = 2$, one would find $C_{\text{ave}} = 0.72$ independently of the number of frequencies n. The particle-averaged cross-correlation resembles the definition of the correlation coefficient ρ between two fluctuation profiles. However, the difference is that C_{ave} compares mass-weighted fluctuations, whereas ρ compares the un-mass-weighted fluctuations. Moreover, C_{ave} takes into account the anisotropy of the fluctuations,[70,71] whereas ρ depends solely on the magnitude of fluctuations. This implies that C_{ave} is sensitive to deviations in the directions of the vibrations between different scales, but ρ is only sensitive to differences in the amplitude of the vibration.

Table 3 compares the cross-correlation between the probability distributions at the different scales of the alpha helix, using imploded Hessians. The correlation between AA/VSA and KT/VSA (ENM/FHVA) is very low, with ln C taking values of -20.8 (-21.0). Because the HNM is our negative control, the cross-correlation between it and all other models should be poor. However, the cross-correlation between HNM and AA is significantly better than the cross-correlation between KT and ENM, indicating significant issues with the metric. By contrast, the particle-averaged correlation C_{ave} in Table 3 gives a similar picture as the correlation coefficient ρ (Table 2) and previous metrics, with reasonable correlations among the imploded AA, KT, and ENM Hessians but poor correlations for HNM. This implies that C_{ave} can be used as a tool to measure the quality of a CG model.

Table 3. Alpha helix—the probability similarity of two scales is quantified by (the logarithm of) the cross-correlation $C(1,2)$ [eq. (49)] and the particle-averaged cross-correlation $C_{\text{ave}}(1,2)$ [eq. (51)] using the imploded mass-weighted Hessians.

ln C(**1**,**2**)	AA	KT	ENM	HNM
AA	0.0	−20.8	−21.0	−38.5
KT		0.0	−85.8	−109.6
ENM			0.0	−89.3
HNM				0.0
C_{ave}(**1**,**2**)	AA	KT	ENM	HNM
AA	1.000	0.727	0.793	0.328
KT		1.000	0.901	0.366
ENM			1.000	0.515
HNM				1.000

Hessian similarity

Single number quantifications of the similarity between two matrices A and B, $s(A, B)$, should be taken with a grain of salt because of significant information loss. Nevertheless, such a metric may still be informative. Hess uses the following similarity definition to compare two square matrices A and B of equal size,[72]

$$s(A, B) = 1 - \frac{\sqrt{\text{tr}(A) + \text{tr}(B) - 2\text{tr}(A^{1/2}B^{1/2})}}{\sqrt{\text{tr}(A) + \text{tr}(B)}}. \tag{52}$$

This expression implies that the largest eigenvalues of the matrices A and B contribute the most to their similarity. As we are most interested in a quantity that is sensitive to the low frequencies, we use the pseudoinverse of the mass-weighted Hessians of two methods **1** and **2** in the formula. A horizontal or vertical mapping should be first applied when the Hessian sizes differ. Reformulating eq. (52) in terms of frequencies and mass-weighted normal modes yields

$$s(\mathbf{1}, \mathbf{2}) = 1 - \frac{\sqrt{\sum_i \left(\omega_i^{\mathbf{1}}\right)^{-2} + \sum_i \left(\omega_i^{\mathbf{2}}\right)^{-2} - 2\sum_{ij} \left(\omega_i^{\mathbf{1}}\omega_j^{\mathbf{2}}\right)^{-1} \left(\tilde{\nu}_i^{\mathbf{1}T}\tilde{\nu}_j^{\mathbf{2}}\right)^2}}{\sqrt{\sum_i \left(\omega_i^{\mathbf{1}}\right)^{-2} + \sum_i \left(\omega_i^{\mathbf{2}}\right)^{-2}}}, \tag{53}$$

where the summations run over the non-zero frequencies. The formula depends on the trace of the pseudoinverse of the mass-weighted Hessian. The quantity $k_B T \text{tr}(\tilde{H}^-)$ represents the total

thermal fluctuations of the particle positions when summed over all particles while assuming that each normal mode coordinate Q_i disposes of an equal amount of energy k_BT. It is the normalization constant $\mathcal{N}_{mw}$ for the thermal fluctuations, as discussed in section Thermal fluctuations [eq. (43)] and reported in Table 2.

The similarity lies between zero and one and combines three effects: the total amount of fluctuations, the "distribution" of frequencies, and the set of normal modes. The total thermal fluctuation effect can be eliminated by dividing the mass-weighted Hessian by $\mathcal{N}_{mw}$. The normalized similarity s_{norm} (**1**, **2**) is then based upon the eigenvalues and eigenvectors of the pseudoinverse of the normalized mass-weighted Hessians, $\tilde{H}^{\mathbf{1}}/\mathcal{N}^{\mathbf{1}}_{mw}$ and $\tilde{H}^{\mathbf{2}}/\mathcal{N}^{\mathbf{2}}_{mw}$, resulting in the expression

$$s_{norm}(\mathbf{1},\mathbf{2}) = 1 - \sqrt{1 - \sum_{ij} \left(\omega_i'^{\mathbf{1}}\omega_j'^{\mathbf{2}}\right)^{-1} \left(\tilde{v}_i^{\mathbf{1}T}\tilde{v}_j^{\mathbf{2}}\right)^2} \quad (54)$$

with the rescaled frequencies $\omega'_i = \omega_i\sqrt{\mathcal{N}_{mw}}$, satisfying $\sum \omega_i'^2 = 1$. Two limiting cases show the two other effects on the similarity. When all normal modes are identical between the models, then $\tilde{v}_i^{\mathbf{1}T}\tilde{v}_i^{\mathbf{2}} = \delta_{ij}$, and the similarity is solely determined by the rescaled frequencies, that is, the total fluctuations $\mathcal{N}_{mw}$ ($\sum \omega_i^{-2}$) are "distributed" over the individual frequencies (ω_i^{-2}). When all frequencies are identical between the models, $\omega_i^{\mathbf{1}} = \omega_i^{\mathbf{2}}$, $\forall i$, the similarity increases with increasing overlap between the set of modes $\tilde{v}_i^{\mathbf{1}}$ and $\tilde{v}_i^{\mathbf{2}}$.

Table 4 presents the comparison between the AA/VSA, the KT/VSA, the ENM/FHVA, and the HNM/FHVA calculations, making use of the imploded mass-weighted Hessians. The similarity is barely altered by normalization when comparing AA with ENM, indicating that the AA and ENM scales have a similar $\mathcal{N}_{mw}$ and thus a similar overall flexibility. The KT model has a better similarity to the AA scale than to the ENM, whereas the HNM has very low similarity to the AA scale. This shows that the similarity is a consistent and discriminative measure to evaluate the performance of a CG model.

Table 4. Alpha helix—similarity s(**1**,**2**) of mass-weighted Hessians [eq. (53)] and similarity s_{norm}(**1**,**2**) of normalized mass-weighted Hessians [eq. (54)] between different scales, after vertical implosion.

s(**1**,**2**)	AA	KT	ENM	HNM
AA	1.000	0.511	0.576	0.150
KT		1.000	0.493	0.108
ENM			1.000	0.225
HNM				1.000
C_{ave}(**1**,**2**)	AA	KT	ENM	HNM
AA	1.000	0.624	0.586	0.201
KT		1.000	0.689	0.219
ENM			1.000	0.276
HNM				1.000

Collectivity of modes

The degree of the collective or global character of modes should be conserved when changing the dimensionality of the NMA. The most global mode has a Cartesian displacement vector with all components equal to $1/\sqrt{n}$. The most local mode has only one component equal to one, whereas all others are zero. As CG models aim to reproduce low frequency modes, the lower part of the spectrum should keep its global character. We report three metrics to evaluate the collectivity of the ith normal mode[28,73]:

$$L_i = n\sum_k y_{i,k}^4, \quad (55)$$

$$LG_i = \frac{n^2}{\left(\sum_k |y_{i,k}|\right)^4}, \quad (56)$$

$$S_i = \frac{\sum_k (-y_{i,k}^2 \ln y_{i,k}^2)}{\ln n}, \quad (57)$$

where $y_{i,k}$ is the kth component of the normalized un-mass-weighted normal mode vector, $y_i = M^{-1/2}\,\tilde{v}_i/|M^{-1/2}\,\tilde{v}_i|$, and n is the length of the vector. L expresses the locality of the mode, LG expresses the lack of globality of a mode, and S expresses the entropy of a mode. None of these metrics are rotationally invariant, so their interpretation is qualitative rather than quantitative. With increasing collectivity, L and LG decrease while S increases. In previous work,[28] the mass-weighted normal mode vector was used. Using y has the advantage that the value of the metrics can be brought to one for the most global mode. The normalization constants n, n^2, and $1/\ln n$ are chosen such that the most global mode gives $L = 1$, $LG = 1$, and $S = 1$, independently of the scale. The most local mode gives $L = n$, $LG = n^2$, and $S = 0$. This shows that S is size-independent, whereas L and LG are size-dependent, especially for the more local modes. Therefore, prior mapping should be applied for L and LG.

We have investigated whether the metrics contain complementary information by calculating L, LG, and S for the AA/FHVA modes (Fig. 7). Not surprisingly, there exists some dependence between the metrics, with a R^2 value between 0.52 (L *vs.* S) and 0.86 (L *vs.* LG) based on the lowest 100 non-zero frequency modes. Nevertheless, there are also modes with ambiguous collective character, which have, for instance, a low locality according to L, but a high lack of globality according to LG.

To compare the mode character at different scales, we have calculated these metrics using FHVA and reordered the modes with increasing L and G and with decreasing S. Because of the size-dependence, the AA results lie closer to the HNM scale than the KT or ENM scale. To bypass this size-dependency, we calculate the metrics after vertical mapping with implosion (section Vertical mapping for coarse-grained models). Figure 8 shows good agreement for the L, LG, and S profiles between the AA, KT, and ENM scales. Overall, the KT modes perform slightly better than the ENM modes, which fits with the picture given by the overlap plots of section Normal modes. The HNM modes have too much local character. Because HNM does not have springs connecting neighboring beads, local motion entails a limited energy penalty and is therefore overly favored. The deviation of the HNM is

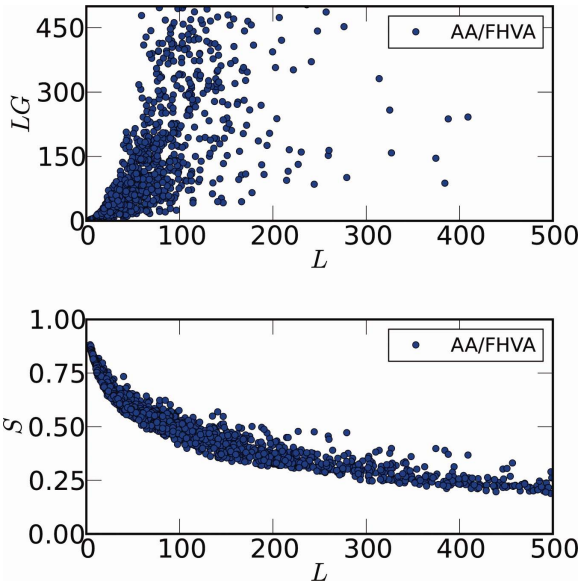

Figure 7. Alpha helix—correlation between the collectivity metrics of the AA/FHVA modes: locality L [eq. (55)], lack of globality LG [eq. (56)], and entropy S [eq. (57)]. [Color figure can be viewed in the online issue, which is available at wileyonlinelibrary.com.]

most apparent in the L and LG profiles but less so in the S profile.

Shape derivatives (dimension-independent)

Shape moments are a convenient mechanism to describe a molecule's spatial extent, which may be thought of a statistical property. The kth moment of a probability distribution $P(X)$ is defined as the expectation value of the kth power of the random variable X and is calculated as:

$$M_{xx\ldots x} = \langle x^k \rangle = \sum_i P(x_i)(x_i)^k, \tag{58}$$

where the sum runs over all possible values x_i for X. Using eq. (58), the expectation coordinates of atom positions can be calculated from all available atom positions. The first-order shape moment of x is defined as:

$$M_x = \sum_A P_A x_A, \tag{59}$$

where the sum runs over all atoms, P_A is the probability, and x_A is the x-coordinate of atom A. M_y and M_z are similarly defined. The probabilities P_A are normalized: $\sum_A P_A = 1$. An equal weight for each atom, $P_A = 1/N_A$, gives the first-order moment the interpretation of the geometric center while mass-weighting, $P_A = m_A / \sum_A m_A$, leads to the center of mass. The second-order moments form a symmetric 3 × 3 matrix; these elements are defined as:

$$M_{xx} = \sum_A P_A x_A^2 \tag{60}$$

$$M_{xy} = \sum_A P_A x_A y_A \tag{61}$$

with similar expressions for the yy, zz, yz, and xz moments. If the probabilities P_A are based on mass, the diagonalization of the second-order shape moments matrix gives the moments of inertia of the molecular system. Likewise, the third-order shape moments form a 3 × 3 × 3 hypermatrix that is symmetric in its indices. The elements are defined as:

$$M_{xxx} = \sum_A P_A x_A^3 \tag{62}$$

$$M_{xxy} = \sum_A P_A x_A^2 y_A \tag{63}$$

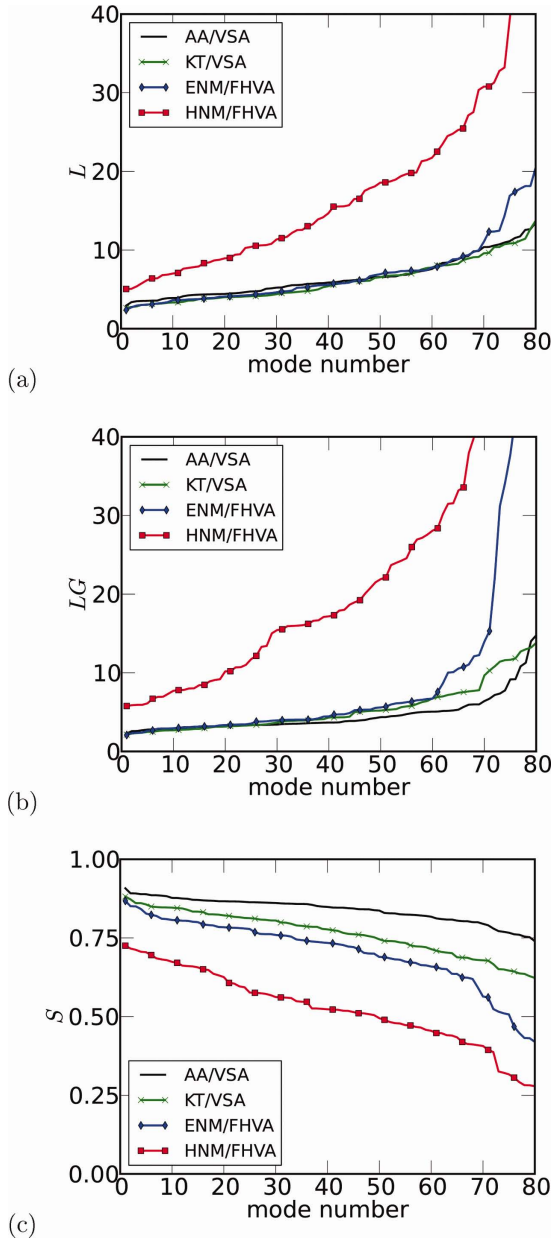

Figure 8. Alpha helix—collectivity character of modes at the AA, KT, ENM, and HNM scale. Modes are ordered with increasing collectivity. a) Locality L as in eq. (55), b) lack of globality LG as in eq. (56), and c) entropy S as in eq. (57). [Color figure can be viewed in the online issue, which is available at wileyonlinelibrary.com.]

$$M_{xyz} = \sum_A P_A x_A y_A z_A \tag{64}$$

and similar expressions follow for the other elements. Third-order elements give information about the skewness of the distribution. For instance, M_{xxx} gives information about the skewness of the atom distribution when projected on the x axis.

The corresponding kth central moments, M^c, are the moments with respect to the first-order moments. For convenience, the first-order moments are assumed to be zero by translating the system to its "center," such that the central moments M^c are no different from the shape moments M. In general, it is not simultaneously possible to put the geometrical center and the center of mass at the origin. Here, we assume that all moments use the masses as weights ($P_A m_A / \sum_A m_A$) and that the center of mass is at the origin.

The moments are calculated with the reference coordinates (x_A^0, y_A^0, z_A^0) at each scale and are compared element-wise to check whether the scales have the same mass distribution (Supporting Information Fig. S.I.18). In CG models, the mass is concentrated in fewer discrete points in space than at the AA scale, where the mass is more evenly distributed over the higher number of interaction centers. This difference in mass distributions should be especially prevalent in moments of systems with significant oblate or prolate character. In this case, a better shape moment correspondence could be obtained by spreading the CG mass over a sphere around the CG particle position. Such a calculation is available with the HOMO (homogeneous spreading) keyword in CHARMM.[56]

A shape derivative, $\partial M/\partial Q_i$, is the derivative of the shape moment with respect to a normal mode coordinate Q_i and expresses how much the shape of a molecule changes as it moves along a normal mode. If $\tilde{v}_i$ denotes the normalized mass-weighted normal mode vector, the shape derivative can be estimated numerically by calculating the moments at two points, r and $r + \Delta r$, where Δr is a displacement along the normal mode vector, $\Delta r = Q_i M^{-1/2} \tilde{v}_i$ [eq. (A2) in Appendix]. The shape derivatives can also be calculated directly from the normal mode vector components, as shown in Appendix. We decided to normalize the moment derivatives to create relative normal mode deformations, because the kth moments and their derivatives scale with system size. A normalized kth-order moment is obtained by division by $r_{\mathrm{gyr}}{}^k$, where the radius of gyration r_{gyr} is calculated from

$$r_{\mathrm{gyr}} = \sqrt{\sum_A P_A (x_A^2 + y_A^2 + z_A^2)} = \sqrt{M_{xx} + M_{yy} + M_{zz}}. \tag{65}$$

The challenge of interpreting the shape derivatives lies in the large amount of data that is generated. For a given scale, there are 3^k moments of order k. Assuming that the center of mass is located at the origin and accounting for symmetry in the elements of the moments, there are six second-order and 10 third-order-independent moments. Each of these 16 moments has a series of shape derivatives with respect to the normal mode coordinates. Comparison across scales, moment orders, individual elements, and specific normal mode derivatives can occur in many ways; here, we present two possibilities.

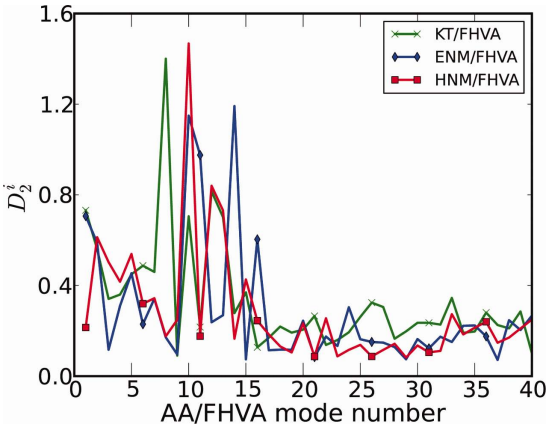

Figure 9. Alpha helix—differences in shape derivatives (in 1.e-3 amu$^{-1/2}$ Å^{-1}) using FHVA. The differences D^i between the AA scale and the KT, ENM, or HNM scales are plotted as a function of the mode number i, here for the second-order moments. The differences fail to detect that HNM is unphysical. [Color figure can be viewed in the online issue, which is available at wileyonlinelibrary.com.]

The first possibility is comparing the shape moment derivatives of scale **1** with those of scale **2** directly. We do this on a mode by mode basis by taking the Frobenius norm of the matrix of differences of shape moment derivatives. For the second-order moments, this is given as:

$$D_2^i(\mathbf{1},\mathbf{2}) = \sqrt{\sum_{j=xx,xy,\ldots} \left(\frac{\partial M_j^{\mathbf{1}}}{\partial Q_i} - \frac{\partial M_j^{\mathbf{2}}}{\partial Q_i} \right)^2}. \tag{66}$$

Calculation of the differences of higher order shape derivatives, D_k^i, follows naturally. In Figure 9, the differences D_2^i in second-order shape derivatives are plotted as a function of the mode number i for the lowest 40 non-zero frequency modes. This plot indicates that the difference in shape derivatives fails to discriminate between reasonable CG models (KT and ENM) and unreasonable CG models (HNM). The underlying reason is that the differences D^i are sensitive to mode ordering, mode mixing, and degeneracy. A CG model might succeed in reproducing the essential protein motions but in a slightly different mode order, thus defeating the diagnostic.

The second possibility is performing a summation over the modes before comparing the shape moment derivatives. This mitigates the differences in mode ordering. Two definitions for the total moment derivative are proposed, one without and one with frequency weighting:

$$D_j^{\mathrm{tot}} = \sum_{i=1}^{n} \left| \frac{\partial M_j}{\partial Q_i} \right|, \tag{67}$$

$$D_j^{\mathrm{tot,fw}} = \sum_{i=1}^{n} \frac{1}{\omega_i^2} \left| \frac{\partial M_j}{\partial Q_i} \right|, \tag{68}$$

for $j = xx,xy,xxx$, and so forth. The total derivative D_j^{tot} represents the total change of M_j when each normal mode coordinate Q_i has an equal mass-weighted displacement. Taking the

absolute value gives the largest change in shape moment, without allowing for destructive interference from mode summation. The total frequency-weighted derivative $D_j^{\mathrm{tot,fw}}$ represents the total change of shape moment M_j when each normal mode coordinate Q_i has an equal average kinetic energy. This weighting naturally gives the low frequency modes a larger contribution to the sum. D_j^{tot} gives only information about the shape profile of the modes, whereas $D_j^{\mathrm{tot,fw}}$ also gives information about the energy distribution.

Figure 10 shows both total derivatives for a range of second and third-order shape moment elements. The total derivatives of the first-order moments are not shown since these are always zero. The total derivatives (Fig. 10a) of the AA, KT, and ENM are very similar with the correct high flexibility in the *x* direction (*xx* and *xxx* moments). The total frequency-weighted derivatives (Fig. 10b) of the AA model and the ENM are in good agreement, whereas the KT model yields a profile with consistently large total shape derivatives. This means that the KT model has the correct relative flexibilities but is too flexible overall. The HNM performs badly for both total derivatives and appears to be too rigid.

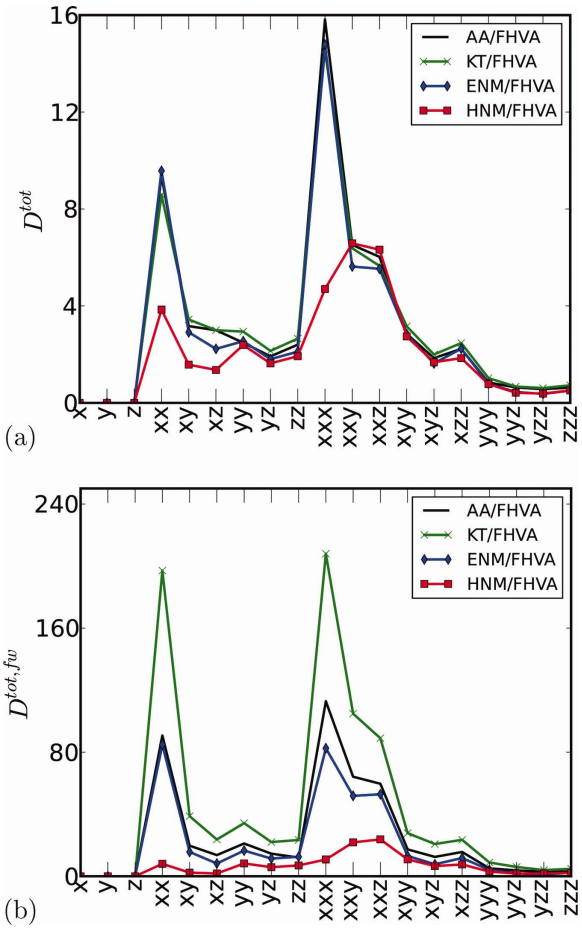

Figure 10. Alpha helix—total shape derivatives using FHVA. The lowest 78 non-zero frequency modes are taken into account. a) Total derivative D^{tot} (in 10^{-3} amu$^{-1/2}$ Å^{-1}) is plotted per element. b) Total frequency-weighted derivative $D^{\mathrm{tot,fw}}$ (in 10^{-3} amu$^{1/2}$ Å mol kcal^{-1}) is plotted per element. [Color figure can be viewed in the online issue, which is available at wileyonlinelibrary.com.]

Projection on spherical harmonics (dimension-independent)

A scale-independent metric can also be designed by solving the NMA equations in a basis set of fixed size. Here, we choose a basis set consisting of the lowest $m = 78$ orthogonal spherical harmonics, excluding the six global translational and rotational vectors. The reduced basis is gathered in a $3N \times m$ matrix *P*, the Hessian and mass matrices are projected on *P* as in eq. (5), and the reduced NMA equations as in eq. (7) are solved. Regardless of the original size, this yields *m* non-zero frequencies and *m* normal modes of length *m*, so that the comparison between scales is now straightforward. The SH-based mapping is also an implosion technique, allowing vertical comparison between CG scales. Although we describe this procedure with a basis set of SH, in principle, any basis set with fixed size could be used. The SH basis set has the advantage that it properly describes structure-independent motions with a collective character; therefore, a reasonable description of the low frequency region is expected.

The derivation for the SH method is analogous to the derivation of the vertical VSA implosion in section Vertical mapping for coarse-grained models. The selected generalized coordinates are the spherical harmonics, which have the same physical appearance for each scale (step 1). Using *P* as a reduced basis set, the size of the Hessian and mass matrix at each scale is reduced to $m \times m$ by projecting the AA and CG mass matrices on the SH basis set, P^{AA} and P^{CG} (step 2),

$$H^{\mathrm{AA/SH}} = (P^{\mathrm{AA}})^T H^{\mathrm{AA}} P^{\mathrm{AA}} \tag{69}$$

$$M^{\mathrm{AA/SH}} = (P^{\mathrm{AA}})^T M^{\mathrm{AA}} P^{\mathrm{AA}} \tag{70}$$

$$H^{\mathrm{CG/SH}} = (P^{\mathrm{CG}})^T H^{\mathrm{CG}} P^{\mathrm{CG}} \tag{71}$$

$$M^{\mathrm{CG/SH}} = (P^{\mathrm{CG}})^T M^{\mathrm{CG}} P^{\mathrm{CG}}. \tag{72}$$

In most cases, the SH mass matrices will differ, and the discrepancy in the kinetic tensors needs be solved by a mass redistribution (step 3). Un-mass-weighting with $M^{\mathrm{AA/SH}}$ followed by re-mass-weighting with $M^{\mathrm{CG/SH}}$, using the $m \times m$ matrix $W = (M^{\mathrm{AA/SH}})^{-1/2}(M^{\mathrm{CG/SH}})^{1/2}$, redistributes the AA masses over the CG degrees of freedom, such that the kinetic tensor $M^{\mathrm{AA/SH}'}$ is equal to the CG kinetic tensor $M^{\mathrm{CG/SH}}$,

$$H^{\mathrm{AA/SH}'} = W^T H^{\mathrm{AA/SH}} W \tag{73}$$

$$M^{\mathrm{AA/SH}'} = W^T M^{\mathrm{AA/SH}} W = M^{\mathrm{CG/SH}}. \tag{74}$$

Similarly, as in eq. (33), the overlap between SH vectors at the AA and CG scales is then calculated as the dot product of the mass-weighted AA/SH and CG/SH mode vectors.

In practice, the AA/FHVA *versus* AA/SH and CG/FHVA *versus* CG/SH are first compared, using *P* for the horizontal mapping (see section Horizontal mapping for reduced basis sets), to determine how well the SH basis set reproduces the FHVA results. Next, the AA/SH and CG/SH can be readily compared without any further mapping. For example, let us compare the AA scale with the ENM scale (KT and HNM in Supporting

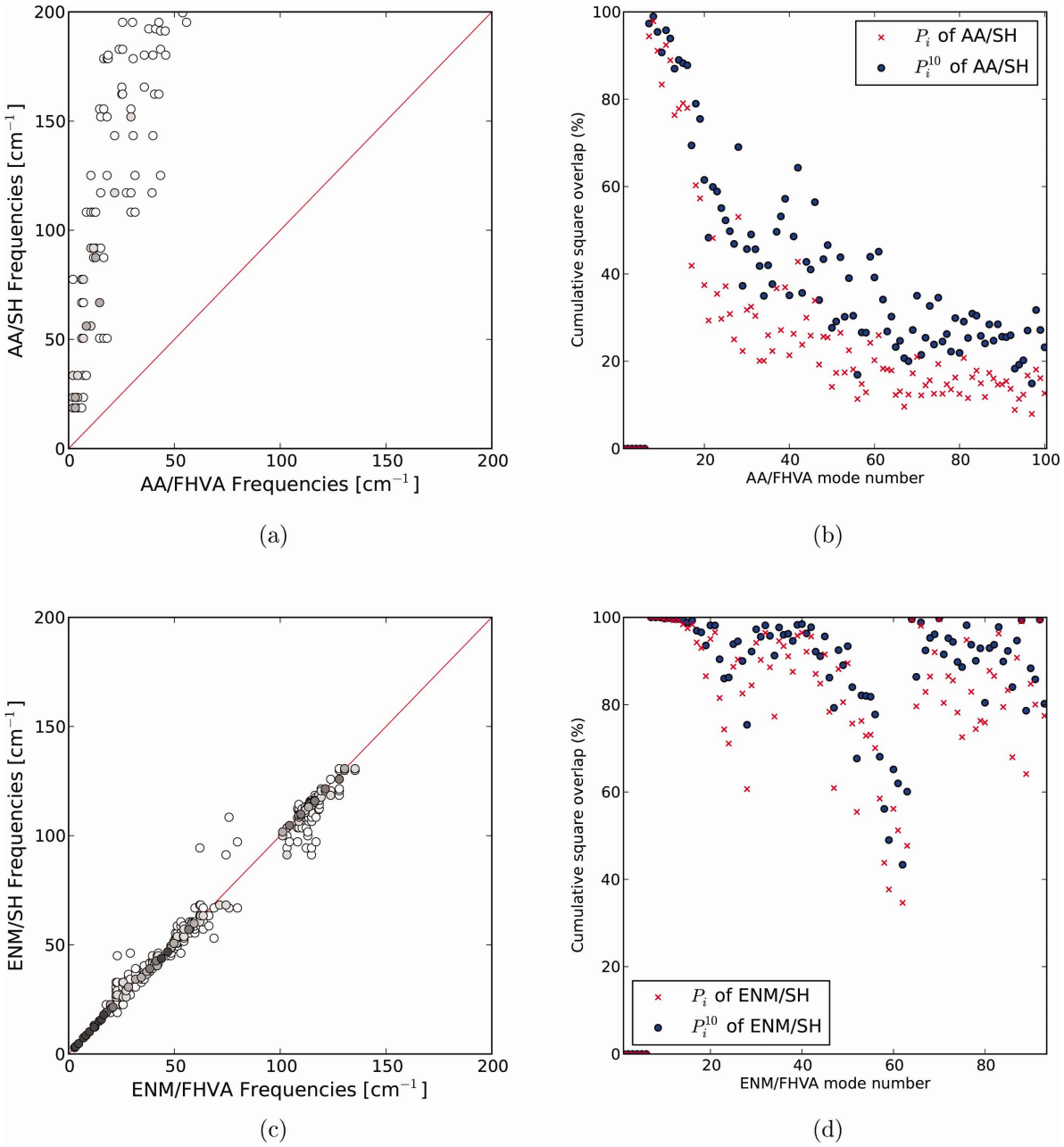

Figure 11. Alpha helix—SH as an alternative to VSA-based Hessian implosion, illustrated with the AA and ENM scale. a) Square overlap: AA/SH overestimates the AA/FHVA frequencies with $f = 7.84$ [fit eq. (34) below 50 cm^{-1}]. b) Cumulative square overlap: reasonable cumulative square overlap below 25 cm^{-1}. c, d) Good agreement between ENM/SH *versus* ENM/FHVA for the frequencies and modes. In the cumulative square overlap plots, the dots represent the total cumulative overlap P_i and the crosses the cumulative overlap of the highest 10 contributions P_i^{10}. [Color figure can be viewed in the online issue, which is available at wileyonlinelibrary.com.]

Information Fig. S.I.19 and S.I.20). For the alpha helix, the ENM/FHVA and ENM/SH have excellent square overlap and cumulative square overlap plots (Figs. 11c and 11d). This is not surprising; at the ENM scale, the SH basis set has only a slightly lower dimension (78) than the FHVA (87 non-zero frequency modes). In contrast, at the AA scale, the square overlap plot between AA/FHVA and AA/SH shows that SH overestimates the frequencies compared to FHVA (Fig. 11a). The SH basis set contains collective spherical harmonic motions that are associated with low frequencies, but the basis set does not allow the bonds and angles within the residues to relax when the helix is deformed. This strain in bonds and angles elevates the SH frequencies. The square overlap of the motions is poor (Fig. 11a), but the cumulative square overlap plot shows a few high values for the lowest 25 modes. After this, the square overlap drops rapidly with increasing mode number (Fig. 11b). This indicates that the SH basis set captures the dynamics of the very lowest eigenmodes only. Therefore, the projection on the SH basis set is not a suitable metric for the comparison of the individual modes at the AA scale. Additional overlap plots between the SH modes of the various scales are provided in Supporting Information (Supporting Information Fig. S.I.21–S.I.25).

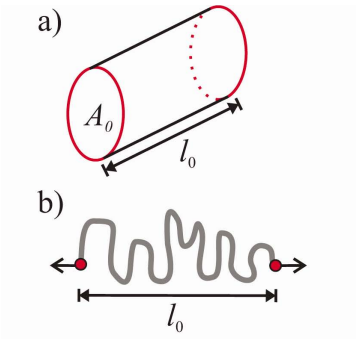

	k [kcal mol^{-1} Å^{-2}]
AA	0.78
KT	0.21
ENM	0.98
HNM	127.99

Figure 12. Elasticity of a molecule. a) A molecule can be seen as a rod with a cross-section A_0 and length l_0. b) The effective force constant k for elongation of the molecule is calculated with VSA by including the two endpoint atoms/beads in the subsystem. The resulting motion resembles pulling apart the endpoints while allowing the rest of the system to relax. (Table) Alpha helix—the effective force constant k calculated at different scales. [Color figure can be viewed in the online issue, which is available at wileyonlinelibrary.com.]

Elastic modulus (dimension-independent)

Single-molecule pulling experiments measure the force required to pull two ends of a molecule apart.[74] The stiffer the molecule, the more force it takes to elongate it. The elasticity of a material is quantified by Young's modulus, which expresses the resistance of the material to elongation under stress. Young's modulus can be calculated as the ratio between the applied stress σ and the strain ε: $Y = \sigma/\varepsilon$. For a protein, Young's modulus can be expressed in terms of force constants using the VSA principle, as demonstrated in the following paragraph.

For a rod with cross-section A_0 and reference length l_0 (Fig. 12), the strain equals $\varepsilon = \Delta l/l_0$ while the stress is written as a function of the applied force $\sigma = F/A_0$. Moreover, the force relates to the force constant $k = \partial^2 E/\partial l^2$ in the harmonic approximation, as Hooke's law applies, $F = -k\Delta l$. Therefore, the Young's modulus of a rod can be written as a function of the force constant,

$$Y = \frac{\sigma}{\varepsilon} = \frac{|F|}{A_0}\frac{l_0}{\Delta l} = k\frac{l_0}{A_0}. \tag{75}$$

The comparison of two scales **1** and **2** is possible by considering the ratio of their Young's moduli. As coarse-graining should not change the shape of the molecule, the cross-section and the reference length should remain unaffected, and the moduli ratio simplifies to a ratio of force constants,

$$\frac{Y^{\mathbf{1}}}{Y^{\mathbf{2}}} = \frac{k^{\mathbf{1}}}{k^{\mathbf{2}}}. \tag{76}$$

The computation of k is inspired by the VSA principle, which lends itself to the derivation of effective force constants. We choose the two end points of the molecule to form the subsystem coordinates (six Cartesian coordinates), whereas all other particles belong to the environment. Following the VSA formalism,[24,25] the Hessian is partitioned into subsystem and environment blocks [similarly to eq. (18)] and an effective 6 × 6 Hessian is derived,

$$H_{\text{eff}} = H_{\text{ss}} - H_{\text{se}}(H_{\text{ee}})^{-1}H_{\text{es}}. \tag{77}$$

Diagonalization of this matrix yields six "principal" force constants. Five of them are zero and represent the three translations and two rotations of the two end points. According to the VSA principle, all environment particles follow the motions of the two subsystem particles instantaneously, so the five zero force constants represent global translations and rotations of the molecule. The sixth force constant represents the stretch of the two end points with respect to each other. The VSA principle dictates that all environment particles meanwhile reconfigure themselves to be force free, so this sixth value is the force constant $k = \partial^2 E/\partial l^2$ of the elongation of the molecule. Note that the effective Hessian in eq. (77) is not mass-weighted. The Young's modulus is a static property that is independent of the mass distribution, and it is solely dependent on the interactions between the particles of the molecule.

To compare the elasticity of the helix at different scales, the C_α (or their CG analog) of the first and last residues are chosen as the subsystem. The calculated force constants in Figure 12 show that the ENM elastic modulus lies close to the AA elastic modulus. In the KT model, the helix becomes too flexible, whereas in the HNM model, the helix is extremely rigid. These results are consistent with results from previous metrics. The high elastic modulus of the HNM model is explained by the fact that the two C_α beads at the end points are connected by a spring with force constant $k = 20$ kcal mol^{-1} Å^{-2}. The elastic modulus thus serves as a sanity check to see whether a model is too rigid or too flexible overall.

Difference in vibrational free energy (dimension-independent)

The transition between multiple states of molecular systems is governed by free energy differences. The vibrational contribution to the free energy can be estimated from the vibrational partition function, Q_{vib}, which is a product of the individual non-zero frequency contributions $q(\omega_i)$,[5,28,75]

$$F_{\text{vib}} = -k_{\text{B}}T\ \ln\ Q_{\text{vib}} = -k_{\text{B}}T\sum_{i=1}^{n}\ln q(\omega_i) \tag{78}$$

The number of contributing modes in this summation may differ between scales, making the direct comparison of the

vibrational free energy, F_{vib}, useless. Nevertheless, an adequate model should still reproduce the differences in free energy between two states, ΔF_{vib}, regardless of scale.

Because the helix test case has only one significant conformation, we have chosen to explore the free energy cost of adding harmonic restraints. Restraining the system is a common first step in umbrella sampling. It is important to accurately calculate the free energy cost, especially when it depends on the conformation. For example, the free energy cost for adding a restraint at the reactant side may not match the energy released by removing the corresponding restraint at the product side.

An energy penalty E^{restr} is added via CHARMM using the CONS command.[56] This harmonically restrains a group of atoms in place during the NMA,

$$E^{restr} = \sum_{A \in group} \kappa m_A \Delta r_A^2, \quad (79)$$

where Δr_A are displacements from the reference structure, and $2\kappa m_A$ is a force constant proportional to the mass.[56,76] The BESTfit option in CHARMM translates and rotates the reference group coordinates to align them with the current coordinates. This restraint does not impose an additional force for translation or rotation of the group; only the internal coordinates of the group are affected. The vibrational frequencies that involve internal coordinate motions are raised. A very high κ approximates treating the group as a rigid mobile block.[16] For a CG model, the summation runs over the beads I in the group and the CG masses m_I should be used. Then a given motion will yield similar energy penalties in the AA and CG scales.

The restraining effect on the spectrum depends on the coupling with the force constants. When the CG force constants resemble the imploded force constants of the AA scale, the AA and CG low frequency spectrum should experience the same restraining effect. Consequently, properties that are dominated by the low frequency contributions, such as the vibrational free energy, may be indicative of unphysical CG force constants when the restraining effect for CG is different than for AA.

For horizontal mapping, the restraining effect depends strongly on the chosen reduced Hessian technique because the reduction [eq. (5)] might project out some of the internal coordinate motion, partially eliminating the restraining effect. For instance, MBH already constrains motions within blocks, so the additional restraints on internal coordinate motion within a block will have no effect.

For each scale of the alpha helix, the vibrational free energy is calculated without restraint at 300 K using FHVA, considering the system as a collection of QM oscillators.[28] Three free energies are calculated: including the first 10, the first 25, and all non-zero modes. These are calculated with the reduced Hessian techniques AA/VSA and AA/MBH. The calculations are repeated using a BESTfit harmonic positional restraint in two schemes. Scheme 1 applies a local restraint: a group consisting of the first six residues is restrained with $\kappa = 0.01$ kcal mol^{-1}amu^{-1}. Scheme 2 applies a weak global restraint: all atoms are restrained with $\kappa = 0.002$ kcal mol^{-1}amu^{-1}.

Table 5. Alpha helix—vibrational free energies F_{vib} of unrestrained helix and free energy shifts ΔF_{vib} of restraint schemes 1 and 2 with contributions of the lowest 10, 25, or all non-zero frequencies, using FHVA, VSA, MBH, and various CG scales.

			Restraint scheme 1		Restraint scheme 2	
Scale	Modes	Unrestrained F_{vib}	ΔF_{vib}	(ΔF_{vib}^{class})	ΔF_{vib}	(ΔF_{vib}^{class})
AA/FHVA	10	−20.45	0.40	(0.40)	2.52	(2.56)
AA/FHVA	25	−40.45	0.89	(0.93)	2.90	(2.96)
AA/FHVA	1650	−189.14	1.34	(1.48)	3.30	(3.45)
AA/VSA	10	−20.30	0.34	(0.34)	2.56	(2.60)
AA/VSA	25	−38.54	0.81	(0.85)	2.97	(3.04)
AA/VSA	87	−67.59	1.17	(1.32)	3.24	(3.39)
AA/MBH	10	−16.83	0.01	(0.01)	1.01	(1.04)
AA/MBH	25	−31.96	0.12	(0.13)	1.13	(1.17)
AA/MBH	180	−76.69	0.20	(0.23)	1.21	(1.27)
KT/FHVA	10	−23.91	0.19	(0.19)	4.49	(4.55)
KT/FHVA	25	−49.22	1.04	(1.08)	5.71	(5.81)
KT/FHVA	177	−154.21	1.80	(1.91)	6.52	(6.69)
ENM/FHVA	10	−19.71	0.12	(0.13)	2.13	(2.17)
ENM/FHVA	25	−39.35	0.34	(0.35)	2.48	(2.53)
ENM/FHVA	87	−83.09	0.49	(0.52)	2.65	(2.73)
HNM/FHVA	10	−15.60	0.57	(0.60)	0.50	(0.52)
HNM/FHVA	25	−36.81	0.98	(1.02)	0.96	(1.00)
HNM/FHVA	87	−81.30	1.20	(1.26)	1.34	(1.42)

All values given are in kcal mol^{-1}. Modes are treated as quantum harmonic oscillators, whereas classical ΔF_{vib}^{class} results are shown in parentheses.

Table 5 shows the unrestrained vibrational free energy F_{vib} and the shift ΔF_{vib} due to the restraint. For horizontal mappings, the ΔF_{vib} values from AA/VSA more closely match those of AA/FHVA. AA/MBH underestimates the free energy shift because part of the free energy cost of adding restraints has already been paid with the use of mobile block constraints.

For vertical mappings, the scheme 1 shifts are too high (HNM), too low (ENM), or unpredictable (KT) with respect to AA. It seems possible for a bad model to produce artificially good agreement, as HNM does a good job of reproducing the AA/FHVA shifts. In contrast, scheme 2 is more revealing. The KT shifts are consistently larger than their AA counterparts, implying the KT model is too flexible. The ENM shifts match the AA shifts, implying approximately correct flexibility of the model. The HNM shifts are much too small, implying the model's global character is much too rigid. All of these results are consistent with findings from previous metrics. In this example, the choice of treating the oscillators classically or quantum mechanically makes little difference. This indicates that high frequency degrees of freedom, well above 200 cm^{-1}, do not play a significant role for the shifts at 300 K. Although scheme 1 is unpredictable for the evaluation of CG models, scheme 2 correctly identifies the flexibilities of all three vertical mappings.

Heat capacity (dimension-independent)

The heat capacity C_v at constant volume expresses how much heat can be absorbed by the particle motions. The translational and rotational degrees of freedom contribute $3R$ to C_v,

where R is the universal gas constant. Each vibration contributes a temperature-dependent term to the molar heat capacity,

$$C_v(T) = 3R + R\sum_i \frac{x_i^2 e^{x_i}}{(e^{x_i}-1)^2} \quad (80)$$

where the sum runs over all non-zero frequencies, and $x_i = \hbar\omega_i/k_B T$ is a dimensionless quantity, with $h = 2\pi\hbar$ the Planck constant. At low temperatures, the scaling behavior of C_v is quantified by a scaling exponent b: $C_v \approx aT^{-b}$. A frequency ω_i only contributes significantly to the heat capacity when the temperature is above the activation temperature $T_i = \hbar\omega_i/k_B$. In practice, this implies frequencies below 200 cm^{-1} are activated at $T = 300$ K. Consequently, the heat capacity is a dimension-independent metric in the temperature range where only the low frequencies contribute, as those low frequencies are typically present in each CG model. At higher temperatures, the higher AA frequencies also contribute to the heat capacity, whereas these local frequencies are absent in the CG models. Therefore, the heat capacity and the scaling exponent become dimension-dependent in the high temperature limit.

Figure 13 compares the alpha helix's heat capacity at different scales using a temperature range from 1 to 10^5 K. Every scale yields $3R$ in the low temperature limit, whereas for high temperatures, the heat capacity saturates to a scale-dependent value of $(3N - 3)R$. For intermediate temperatures, a linear fit on a log–log plot $\ln C_v = \ln a - b \ln T$ reveals the scaling exponent b. Because all CG models should reproduce low frequencies, we want a metric that is sensitive in this range. We determine the slope of the curve at 30 K, as the activated frequencies contributing to the heat capacity are on the order of 20 cm^{-1} at this temperature. The scaling exponent is 1.021, 1.014, and 1.078 at the AA, KT, and ENM scales, respectively. Thus, the difference in flexibility of the KT model is not recognized. In contrast, HNM drastically overestimates the scaling exponent (2.766).

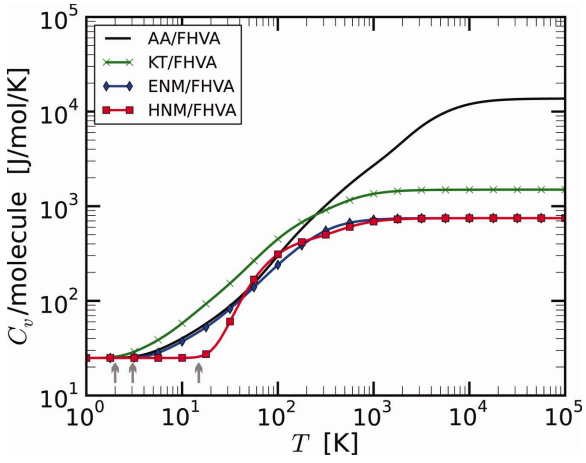

Figure 13. Alpha helix—heat capacity C_v per molecule as a function of temperature calculated at the AA, KT, ENM, and HNM scale [eq. (80)]. Gray arrows indicate the activation temperature T_{act} in the low temperature region; AA and ENM have almost equal activation temperature. [Color figure can be viewed in the online issue, which is available at wileyonlinelibrary.com.]

Sometimes, evaluating the model flexibility using a scaling exponent may fail. In this case, the C_v curves of different scales may cross each other (Fig. 13), such that, according to the mean value theorem, the slopes of the curves are necessarily identical at some specific temperature point. Because the slope lacks robustness with respect to temperature, it is good practice to inspect the complete C_v plot instead of drawing conclusions from a scaling exponent estimation calculated at a single temperature point.

The complete curve clearly gives more information about the frequency distribution. A temperature scan accurately samples the activation temperatures, and therefore the activation frequencies, of the various scales. In particular, inspection of the low-frequency region in Figure 13 reveals the KT curve activates at a lower temperature than for any other scale ($T_{act} \approx 2$ K $\rightarrow$ 1 cm^{-1}). This in turn implies that the KT model is more flexible than the other models. Similarly, the AA and ENM curves activate together ($T_{act} \approx 3$ K $\rightarrow$ 2 cm^{-1}, ENM at a slightly higher temperature than AA), implying these models have a similar flexibility to each other, yet are more flexible than the HNM. Finally, the HNM curve activates at the highest temperature ($T_{act} \approx 15$ K $\rightarrow$ 7.5 cm^{-1}), indicating it is the least flexible of the models. From Figure 13, we may conclude the following regarding the relative flexibilities of the models: KT $>$ AA $\approx$ ENM $>$ HNM.

Illustration with a Globular Protein

To show the general utility of our methods, we apply them to a real globular protein: the GA module of the poly(A)-binding protein, 1PRB (Fig. 14, computational details in section Test Cases: Alpha Helix and Globular Protein). The interesting coordinates q_s are the C_α positions. Implosion of the AA (AA/VSA) and KT (KT/VSA) scales reduces the number of frequencies to 141, the same number as for ENM/FHVA and HNM/FHVA. 1PRB is a realistic illustration where no rescaling of the ENM force constants is done to improve resemblance with the AA scale. This is in contrast to the ENM parameters of the alpha helix, which are fitted to reproduce its lowest 10 frequencies.[62] The AA coordinates are obtained by energy minimization of the PDB structure, whereas the KT, ENM, and HNM coordinates are taken from the PDB structure. Consequently, the C_α positions differ between the AA scale and the CG scales. In contrast, the setup of the alpha helix test case results in identical C_α positions for all scales. Thus, our 1PRB results should be slightly worse than our alpha helix results.

The NMA comparison was performed between the different scales in a manner consistent with the alpha helix system. Most of the graphical and numerical results have been deferred to Supporting Information. From this analysis, we conclude that with respect to the AA scale, the KT model is too flexible, the ENM is too rigid, and true to its name, the HNM is horrible and far too rigid. The frequency underestimation by KT is illustrated by plotting the KT/FHVA frequencies with respect to the reference AA/FHVA frequencies (Fig. 15).

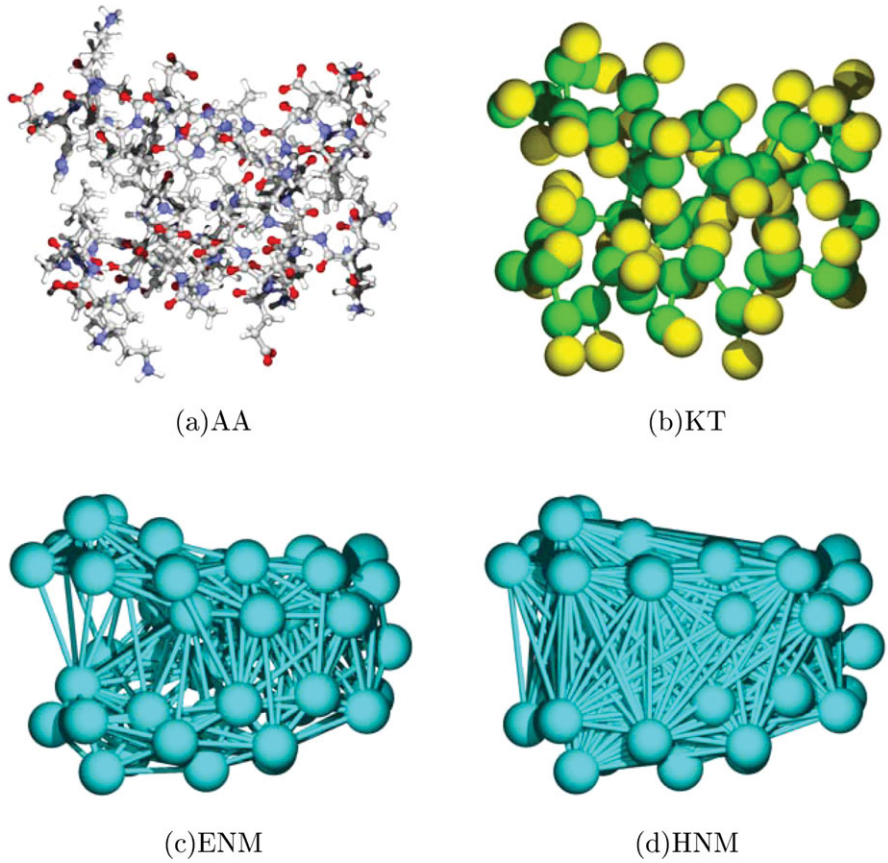

Figure 14. The 1PRB system is described at the AA scale and with three CG models (KT, ENM, and HNM).

The proportionality factors with respect to AA [eq. (34), fit below 50 cm^{-1}] are $f = 0.58$ for KT, $f = 1.53$ for ENM, and $f = 2.75$ for HNM. The CG scales reproduce the AA spectrum only moderately, such that most metrics only yield mediocre scores.

The quality of the VSA-based implosion, which is necessary to use size-dependent metrics with the AA and KT scales, is investigated by comparing FHVA with the full-size VSA normal mode vectors. Figure 16 shows strong square overlap [eq. (37)] in the low-frequency region, where most values lie on the diagonal. The cumulative overlap [eq. (38)] gradually decreases at higher frequencies. Given the huge reduction in degrees of freedom, the imploded quantities may be considered as valid approximations to those of the full Hessian.

The trend of overestimation and underestimation of frequencies is seen in the square overlap plots between imploded AA vectors and CG vectors (see Supporting Information). Numerically, the elasticity gives a force constant $k = 9.5$ kcal mol^{-1} $Å^{-2}$ at the AA scale, whereas the KT, the ENM, and the HNM scales give 2.9, 18.9, and 437.8 kcal mol^{-1} $Å^{-2}$, respectively. The difference in flexibility is also reflected in the total amount of fluctuations $\mathcal{N}$, the total amount of mass-weighted fluctuations $\mathcal{N}_{mw}$, the heat capacity C_v at low temperature, the (normalized) Hessian similarity s_{norm} (s), and the probability similarity by means of the cross-correlation C or C_{ave} (see Supporting Information). The difference in the nature of the modes is visible in the overlap plots, the locality L, the lack of globality LG, the entropy S, and the normalized thermal fluctuations profile (see Supporting Information). These latter profiles locate a hot spot at residue 16 when using AA. The ENM calculations also identify this region as a hot spot, where the KT does not. The HNM is densely coupled, barely allowing for any local thermal fluctuations, and therefore neglects to detect any hot spots.

The shape moments M [eq. (58)] in Figure 17 permit visualization of the mass distributions. The geometry optimization at the AA scale causes the deviations of the *xxy* and *yyy* shape moments. ENM and HNM use the same coordinates and bead masses. KT uses these coordinates as well, but some minor deviations arise from regrouping the mass to the C_α bead and the side-chain bead. In a sense, the AA and the KT masses are more spread out in space compared to the coarser ENM and HNM models, causing minor differences in the shape moments. However, Figure 17 shows that the effect of condensing mass in CG models is smaller than the effect of geometry optimization.

Conclusions

We have described mapping schemes and metrics useful for comparing Hessians and normal modes of systems at different scales. For reduced Hessian techniques such as VSA or MBH, the horizontal mapping makes use of a well-defined projection matrix. For CG models such as KT or ENM, a vertical mapping scheme was developed based on the VSA principle,

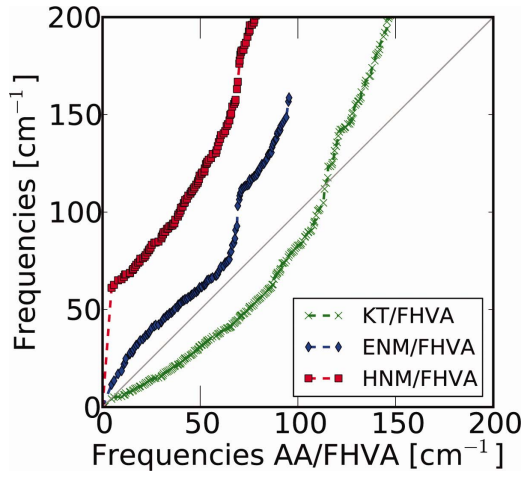

Figure 15. 1PRB—frequencies in cm^{-1} calculated with the full Hessian (FHVA) at the KT, ENM, and HNM scales *versus* the AA scale. [Color figure can be viewed in the online issue, which is available at wileyonlinelibrary.com.]

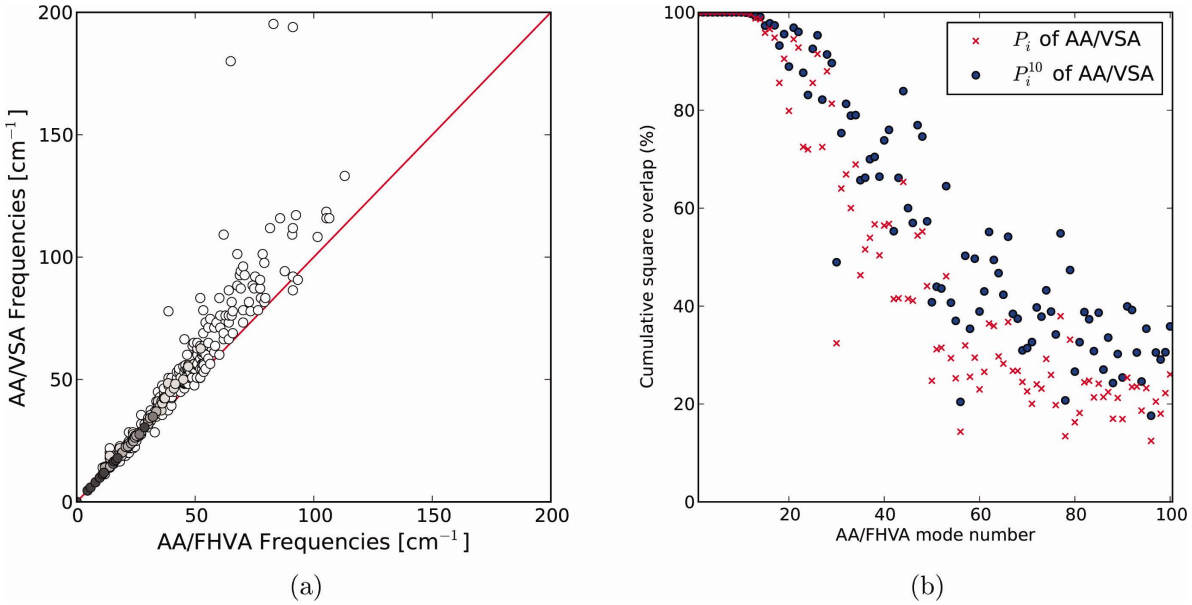

Figure 16. 1PRB—verification that the implosion with VSA reproduces the lower spectrum well. a) Square overlap plot of AA/FHVA and AA/VSA shows high overlaps for low frequencies. Darker dots represent higher squared overlaps; values below 0.05 are not printed. b) Cumulative square overlap of AA/FHVA and AA/VSA shows high values for low frequencies, but it rapidly decreases at higher frequencies. Dots represent the total cumulative overlap P_i and crosses represent the cumulative overlap of the highest 10 contributions P_i^{10}. Data for KT/FHVA *versus* KT/VSA in Supporting Information. [Color figure can be viewed in the online issue, which is available at wileyonlinelibrary.com.]

which leads to an effective Hessian in terms of a set of interesting generalized coordinates. The same VSA implosion is applied to the mass matrix, followed by a mass redistribution, such that the imploded AA vectors have the same kinetic tensor as the CG vectors. Only then is a systematic mode comparison possible, as mass plays a role in any time-dependent quantity—in this case the vibrational frequencies and mode vectors.

After applying the implosion technique described above, it is straightforward to compare modes from different scales by constructing overlap plots. We considered additional metrics. Some of these, such as Hessian similarity and collectivity, are dimension-dependent, whereas shape derivates, projection onto the SH basis set, elastic modulus, vibrational free energy differences, and heat capacity are dimension-independent. From these metrics, the square overlap plot for direct mode comparison contains the most detailed information, being two-dimensional. The frequency plot, the density of states profile, the cumulative square overlap plot, the fluctuation profile, the shape derivatives profile, and the heat capacity plot are one-dimensional, so they still give reasonably detailed information. The thermal fluctuations profile gives information about the spatial distribution of the energy. The total shape derivatives indicate which directions are most flexible, and the total frequency-weighted shape derivatives indicate which directions are most flexible in thermal equilibrium. The elastic modulus, the probability similarity, the Hessian similarity, the difference in vibrational free energy, and the heat capacity scaling exponent condense the mode comparison into a single number, rendering these tools very compact.

The above mapping procedures and metrics are here studied for NMA, but the same type of analysis is applicable to matrices obtained from instantaneous normal modes (INM)[77] or from quasi-harmonic analysis (QHA),[30] also referred to as essential dynamics[78] and principal component analysis. In the INM, the Hessian is evaluated during a molecular dynamics trajectory when the structure is not necessarily at a stationary point on the energy surface. In the QHA, the Hessian is replaced by the pseudoinverse of the correlation matrix of the atom positions during a molecular dynamics run, also known as the compliance matrix.[79]

The mapping of forces and Hessians has been previously discussed and applied by the groups of Eom, Voth, and Zhou[38,53,80] for the purpose of fitting new force fields for CG

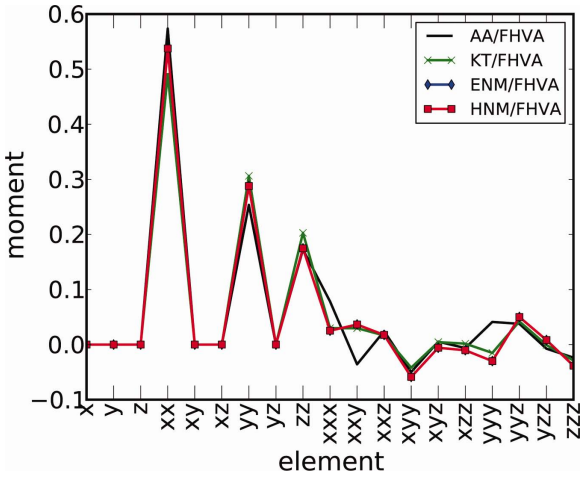

Figure 17. 1PRB—first-, second-, and third-order shape moments M [eq. (58)], normalized by r_{gyr}, r_{gyr}^2, and r_{gyr}^3, respectively. At each scale, the 1PRB protein is aligned along its principal axes. [Color figure can be viewed in the online issue, which is available at wileyonlinelibrary.com.]

Table 6. The metrics are categorized according to their effectiveness: '+++' metrics give semiquantitative information about the flexibility, '++' metrics give basic qualitative information about the flexibility, '+' metrics discriminate the HNM but nothing else, '−' metrics carry barely any information.

Metric symbol	Effectiveness	Section
f	+++	Frequencies
O_{ij}	+++	Normal modes
$\mathcal{N}$	+++	Thermal fluctuations
$\mathcal{N}_{mw}$	+++	Thermal fluctuations
Y	+++	Elastic modulus (dimension-independent)
ΔF^2_{vib}	+++	Difference in vibrational free energy (dimension-independent)
P_i	++	Normal modes
$\langle \Delta r_f^2 \rangle$	++	Thermal fluctuations
$D_j^{tot,fw}$	++	Shape derivatives (dimension-independent)
$T_{act}(C_v)$	++	Heat capacity (dimension-independent)
$P_i^{(k)}$	+	Normal modes
$\langle \Delta r_f^2 \rangle / k_B T \mathcal{N}$	+	Thermal fluctuations
ρ	+	Thermal fluctuations
C_{ave}	+	Probability similarity
s	+	Hessian similarity
s_{norm}	+	Hessian similarity
L	+	Collectivity of modes
LG	+	Collectivity of modes
D_j^{tot}	+	Shape derivatives (dimension-independent)
$b(C_v)$	+	Heat capacity (dimension-independent)
$g(\omega)$	−	Frequencies
ln C	−	Probability similarity
S	−	Collectivity of modes
D_k^i	−	Shape derivatives (dimension-independent)
SH	−	Projection on SH (dimension-independent)
ΔF^1_{vib}	−	Difference in vibrational free energy (dimension-independent)

For names and definitions we refer to the text in the corresponding subsections (last column).

models, where the VSA principle was applied to construct the effective Hessian. But the potential energy surface does not solely determine the behavior of a molecular system; the mass matrix is also needed to describe the dynamics. Our mapping is a continuation of the effort to validate CG models by extending the validation of the potential energy to the validation of the mass matrix. We suggest that the focus of future CG development also includes 'mass matrix matching' based on NMA mapping, besides force matching and Hessian matching.

To test both the implosion mapping and the power of the metrics, the normal modes of a 31 residue alpha helix and a globular albumin-binding domain of protein G are calculated at the AA, KT, ENM, and HNM scales. These techniques could also be applied to multiscale models, that is, where part of the system is described at the AA scale and part of the system at a CG scale. Multiscale models are ideal to cover multiple length and time scales but need thorough validation, of which our NMA mapping could be part.

In our helix test case, Hessian implosion is applied to the AA and KT scale using the C_α positions as the subsystem coordinates in VSA. The overlap plots between the FHVA and imploded vectors compare well in the low-frequency region, indicating that the implosion is a valid approach. Our analysis with the metrics indicates that the flexibility of ENM lies closely to that of AA, whereas KT is too flexible (based on frequencies, overlap, total thermal fluctuations, total frequency-weighted difference in shape derivatives, elastic modulus, difference in vibrational free energy, and heat capacity). However, the imploded AA modes agree slightly better with the KT modes than with the ENM modes (based on overlap, Hessian similarity, collectivity of modes, and lack of globality of modes). HNM is found to perform badly both for the reproduction of the flexibility and the modes. In our larger 1PRB system, the metrics are able to reveal that KT is too flexible, ENM is too rigid, and HNM again performs badly.

Based on these two test cases, we summarize the effectiveness of the metrics in Table 6, which may serve as a guideline when comparing reduced Hessian techniques or CG scales. The following metrics successfully discriminate between the good and bad models: frequencies, square overlap plot, total (mass-weighted) thermal fluctuations, elastic modulus, vibrational free energy difference in scheme 2, cumulative square overlap plot, thermal fluctuation profile, total frequency-weighted shape derivatives, and activation temperature of heat capacity. The following metrics recognize the HNM as a bad model but give little qualitative information about the flexibility: normalized thermal fluctuation profile, correlation coefficient, particle-averaged cross-correlation, (normalized) Hessian similarity, globality of modes, lack of globality of modes, total shape derivatives, and scaling exponent of heat capacity. In contrast, the density of states profile, cross-correlation, entropy of modes, differences in shape derivative, projection on a SH basis set, and vibrational free energy difference in scheme 1 are metrics that poorly differentiate the unphysical model.

Acknowledgments

A.G. is postdoctoral Fellow of the Fund for Scientific Research—Flanders (FWO). This research was in part supported by the intramural research program of the NIH, National Heart, Lung, and Blood Institute.

Appendix: Analytical Calculation of Shape Derivatives

Assume a moment of order $k = k_x + k_y + k_z$, defined as:

$$M_{x^{k_x}y^{k_y}z^{k_z}} = \sum_A P_A x_A^{k_x} y_A^{k_y} z_A^{k_z} \tag{A1}$$

where the sum runs over all atoms A, P_A is the probability, and x_A,y_A,z_A are the Cartesian coordinates of atom A. The Cartesian coordinates are written as a function of the normal mode coordinates Q_i by applying a linear transformation

$$x_A(Q) = x_A^0 + \sum_i Q_i \frac{1}{\sqrt{m_A}} \tilde{v}_{i,Ax} \tag{A2}$$

and similarly for y_A,z_A. Here the sum runs over all modes i, x_A^0 is the coordinate at the reference position and $\tilde{v}_{i,Ax}$ is the x-coordinate of the A atom displacement in the ith normalized mass-weighted normal mode vector $\tilde{v}_i$. The shape derivative of the kth-order moment with respect to Q_i is obtained by applying the chain rule,

$$\frac{\partial M}{\partial Q_i} = \sum_A P_A \left(\frac{\partial (x_A^{k_x} y_A^{k_y} z_A^{k_z})}{\partial x_A} \frac{\partial x_A}{\partial Q_i} + \frac{\partial (x_A^{k_x} y_A^{k_y} z_A^{k_z})}{\partial y_A} \frac{\partial y_A}{\partial Q_i} + \frac{\partial (x_A^{k_x} y_A^{k_y} z_A^{k_z})}{\partial z_A} \frac{\partial z_A}{\partial Q_i} \right) \tag{A3}$$

$$= \sum_A P_A \left(k_x x_A^{k_x - 1} y_A^{k_y} z_A^{k_z} v_{i,Ax} + k_y x_A^{k_x} y_A^{k_y - 1} z_A^{k_z} v_{i,Ay} + k_z x_A^{k_x} y_A^{k_y} z_A^{k_z - 1} v_{i,Az} \right) \tag{A4}$$

where $v_{i,Ax} = m_A^{-1/2}\, \tilde{v}_{i,Ax}$ (etc.) is the Ax component of the unmass-weighted mode vector. These analytical derivatives agree well with the numerical derivatives of section Shape derivatives. Deviations of the numerical derivatives can occur when the finite step in Q_i is too large (anharmonic effects) or when the step is too small (numerical accuracy).

Keywords: effective Hessian · NMA · normal mode analysis · vibrational analysis · chemical kinetics · entropy · free energy · coarse-grained models · coarse-graining · kinetic tensor · elastic network model · heat capacity · CG

How to cite this article: A. Ghysels, B.T. Miller, F.C. Pickard IV, B.R. Brooks, *J. Comput. Chem.* **2012,** *33,* 2250–2275. DOI: 10.1002/jcc.23076

Additional Supporting Information may be found in the online version of this article.

[1] L. Mouawad, D. Perahia, *Biopolymers* **1993**, *33,* 599.
[2] M. Reiher, J. Neugebauer, *Phys. Chem. Chem. Phys.* **2004**, 4621.
[3] C. R. Jacob, M. Reiher, *J. Chem. Phys.* **2009**, *130,* 15.
[4] Q. Cui, I. Bahar, Normal Mode Analysis: Theory and Applications to Biological and Chemical Systems; Mathematical and Computational Biology Series; Chapman & Hall/CRC, Taylor & Francis Group: Boca Raton, FL, **2006**.
[5] D. A. Mc Quarrie, J. D. Simon, Physical Chemistry—A Molecular Approach; University Science Books: Sausalito, California, **1997**; pp. 1075–1079.
[6] P. R. Schreiner, H. P. Reisenauer, F. C. Pickard, IV, A. C. Simmonett, W. D. Allen, E. Matyus, A. G. Csaszar, *Nature* **2008**, *453,* 906.
[7] N. Go, T. Noguti, T. Nishikawa, *Proc. Natl. Acad. Sci. USA* **1983**, *80,* 3696.
[8] B. R. Brooks, M. Karplus, *Proc. Natl. Acad. Sci.* **1983**, *80,* 6571.
[9] O. Marques, Y. H. Sanejouand, *Proteins* **1995**, *23,* 557.
[10] D. Ben-Avraham, M. M. Tirion, *Biophys. J.* **1995**, *68,* 1231.
[11] W. J. Zheng, B. R. Brooks, *Biophys. J.* **2006**, *90,* 4327.
[12] J. D. Head, *Int. J. Quantum Chem.* **1997**, *65,* 827.
[13] H. Li, J. H. Jensen, *Theor. Chem. Acc.* **2002**, *107,* 211.
[14] N. A. Besley, K. A. Metcalf, *J. Chem. Phys.* **2007**, *126,* 035101.
[15] V. Van Speybroeck, J. Van der Mynsbrugge, M. Vandichel, D. Hemelsoet, A. Ghysels, G. B. Marin, M. Waroquier, *J. Am. Chem. Soc.* **2011**, *133,* 888.
[16] A. Ghysels, D. Van Neck, V. Van Speybroeck, T. Verstraelen, M. Waroquier, *J. Chem. Phys.* **2007**, *126,* 224102.
[17] A. Ghysels, D. Van Neck, M. Waroquier, *J. Chem. Phys.* **2007**, *127,* 164108.
[18] A. Ghysels, V. Van Speybroeck, E. Pauwels, D. Van Neck, B. R. Brooks, M. Waroquier, *J. Chem. Theory Comput.* **2009**, *5,* 1203.
[19] W. F. Vangunsteren, H. J. Berendsen, *Mol. Phys.* **1977**, *34,* 1311.
[20] P. Durand, G. Trinquier, Y. H. Sanejouand, *Biopolymers* **1994**, *34,* 759.
[21] F. Tama, F. X. Gadea, O. Marques, Y. H. Sanejouand, *Proteins: Struct. Funct. Genet.* **2000**, *41,* 1.
[22] F. Tama, Y. H. Sanejouand, *Protein Eng.* **2001**, *14,* 1.
[23] A. Ghysels, D. Van Neck, V. Van Speybroeck, B. R. Brooks, M. Waroquier, *J. Chem. Phys.* **2009**, *130,* 084107.
[24] W. J. Zheng, B. R. Brooks, *Biophys. J.* **2005**, *89,* 167.
[25] H. L. Woodcock, W. J. Zheng, A. Ghysels, Y. H. Shao, J. Kong, B. R. Brooks, *J. Chem. Phys.* **2008**, *129,* 214109.
[26] J. Hafner, W. Zheng, *J. Chem. Phys.* **2009**, *130,* 194111.
[27] A. Ghysels, V. Van Speybroeck, E. Pauwels, S. Catak, B. R. Brooks, D. Van Neck, M. Waroquier, *J. Comput. Chem.* **2010**, *31,* 994.
[28] B. R. Brooks, D. Janezic, M. Karplus, *J. Comput. Chem.* **1995**, *16,* 1522.
[29] D. Janezic, B. R. Brooks, *J. Comput. Chem.* **1995**, *16,* 1543.
[30] D. Janezic, R. M. Venable, B. R. Brooks, *J. Comput. Chem.* **1995**, *16,* 1554.
[31] B. A. De Moor, A. Ghysels, M. F. Reyniers, V. Van Speybroeck, M. Waroquier, G. B. Marin, *J. Chem. Theory Comput.* **2011**, *7,* 1090.
[32] K. Hemelsoet, A. Ghysels, D. Mores, K. De Wispelaere, V. Van Speybroeck, B. M. Weckhuysen, M. Waroquier, *Catal. Today* **2011**, *177,* 12.
[33] H. Lin, D. G. Truhlar, *Theor. Chem. Acc.* **2007**, *117,* 185.
[34] Q. Cui, M. Karplus, *J. Chem. Phys.* **2000**, *112,* 1133.
[35] A. Ghysels, H. L. Woodcock, III, J. D. Larkin, B. T. Miller, Y. Shao, J. Kong, D. Van Neck, V. Van Speybroeck, M. Waroquier, B. R. Brooks, *J. Chem. Theory Comput.* **2011**, *7,* 496.
[36] S. Izvekov, M. Parrinello, C. J. Burnham, G. A. Voth, *J. Chem. Phys.* **2004**, *120,* 10896.
[37] S. Izvekov, G. A. Voth, *J. Phys. Chem. B.* **2005**, *109,* 2469.
[38] W. G. Noid, J. W. Chu, G. S. Ayton, V. Krishna, S. Izvekov, G. A. Voth, A. Das, H. C. Andersen, *J. Chem. Phys.* **2008**, *128,* 244114.
[39] E. P. O'Brien, G. Ziv, G. Haran, B. R. Brooks, D. Thirumalai, *Proc. Natl. Acad. Sci. USA* **2008**, *105,* 13403.
[40] D. Thirumalai, E. P. O'Brien, G. Morrison, C. Hyeon, *Annu. Rev. Biophys.* **2010**, *39,* 159.
[41] V. Tozzini, *Curr. Opin. Struct. Biol.* **2005**, *15,* 144.
[42] M. M. Tirion, *Phys. Rev. Lett.* **1996**, *77,* 1905.
[43] I. Bahar, A. R. Atilgan, B. Erman, *Fold. Des.* **1997**, *2,* 173.
[44] K. Hinsen, *Proteins: Struct. Funct. Genet.* **1998**, *33,* 417.
[45] K. Hinsen, A. J. Petrescu, S. Dellerue, M. C. Bellissent-Funel, G. R. Kneller, *Chem. Phys.* **2000**, *261,* 25.
[46] H. Gohlke, M. F. Thorpe, *Biophys. J.* **2006**, *91,* 2115.
[47] T. Haliloglu, I. Bahar, B. Erman, *Phys. Rev. Lett.* **1997**, *79,* 3090.
[48] A. R. Atilgan, S. R. Durell, R. L. Jernigan, M. C. Demirel, O. Keskin, I. Bahar, *Biophys. J.* **2001**, *80,* 505.
[49] W. Zheng, *Biophys. J.* **2008**, *94,* 3853.
[50] Y. Ueda, H. Taketomi, N. Gō, *Biopolymers* **1978**, *17,* 1531.
[51] D. K. Klimov, D. Thirumalai, *J. Chem. Phys.* **1998**, *109,* 4119.
[52] D. K. Klimov, D. Thirumalai, *Proc. Natl. Acad. Sci. USA* **2000**, *97,* 2544.
[53] K. Eom, S. C. Baek, J. H. Ahn, S. Na, *J. Comput. Chem.* **2007**, *28,* 1400.
[54] L. Zhou, A. Siegelbaum, *Biophys. J.* **2008**, *94,* 3461.
[55] P. B. Harbury, T. Zhang, P. S. Kim, T. Alber, *Science* **1993**, *262,* 1401.
[56] B. R. Brooks, C. L. Brooks III, A. D. Mackerell, Jr., L. Nilsson, R. J. Petrella, B. Roux, Y. Won, G. Archontis, C. Bartels, S. Boresch, A. Caflisch, L. Caves, Q. Cui, A. R. Dinner, M. Feig, S. Fischer, J. Gao, M. Hodoscek, W. Im, K. Kuczera, T. Lazaridis, J. Ma, V. Ovchinnikov, E. Paci, R. W. Pastor, C. B. Post, J. Z. Pu, M. Schaefer, B. Tidor, R. M. Venable, H. L. Woodcock, X. Wu, W. Yang, D. M. York, M. Karplus, *J. Comput. Chem.* **2009**, *30,* 1545.
[57] A. D. MacKerell, Jr., M. Feig, C. L. Brooks, III, *J. Comput. Chem.* **2004**, *25,* 1400.
[58] B. T. Miller, R. P. Singh, J. B. Klauda, M. Hodoscek, B. R. Brooks, H. L. Woodcock, III, *J. Chem. Inf. Mod.* **2008**, *48,* 1920.
[59] A. Ghysels, T. Verstraelen, K. Hemelsoet, V. Van Speybroeck, M. Waroquier, *J. Chem. Inf. Mod.* **2010**, *50*, 1736.
[60] B. Brooks, M. Karplus, *Proc. Natl. Acad. Sci. USA* **1985**, *82,* 4995.
[61] S. Miyazawa, R. L. Jernigan, *J. Mol. Biol.* **1996**, *256,* 623.
[62] H. L. Woodcock, B. T. Miller, M. Hodoscek, A. Okur, J. D. Larkin, J. W. Ponder, B. R. Brooks, *J. Chem. Theory Comput.* **2011**, *7,* 1208.

[63] M. de Château, L. Björck, *J. Biol. Chem.* **1994**, *269,* 12147.
[64] M. U. Johansson, M. de Château, M. Wikström, S. Forsén, T. Drakenberg, L. Björck, *J. Mol. Biol.* **1997**, *266,* 859.
[65] T. Wang, Y. Zhu, F. Gai, *J. Phys. Chem. B* **2004**, *108,* 3694.
[66] R. B. Best, G. Hummer, *Proc. Natl. Acad. Sci. USA* **2010**, *107,* 1088.
[67] S. Takada, *Proteins* **2001**, *42,* 85.
[68] W. Zheng, J. C. Liao, B. R. Brooks, S. Doniach, *Proteins* **2007**, *67,* 886.
[69] R. Carb, L. Leyda, M. Arnau, *Int. J. Quantum Chem.* **1980**, *17,* 1185.
[70] E. A. Merritt, *Acta Crystallogr.* **1999**, *D55,* 1997.
[71] D. Riccardi, Q. Cui, G. N. Philips, Jr., *Biophys. J.* **2009**, *96,* 464.
[72] B. Hess, *Phys. Rev. E* **2002**, *65,* 031910.
[73] S. F. Lienin, R. Bruschweiler, *Phys. Rev. Lett.* **2000**, *84,* 5439.
[74] S. Kumar, M. S. Li, *Phys. Rep.* **2010**, *486,* 1.
[75] A. Ghysels, V. Van Speybroeck, T. Verstraelen, D. Van Neck, M. Waroquier, *J. Chem. Theory Comput.* **2008**, *4,* 614.
[76] J. W. Chu, B. L. Trouta, B. R. Brooks, *J. Chem. Phys.* **2003**, *119,* 12708.
[77] R. M. Stratt, *Acc. Chem. Res.* **1995**, *28,* 201.
[78] A. Amadei, A. B. M. Linssen, H. J. C. Berendsen, *Proteins* **1993**, *17,* 412.
[79] K. Brandhorst, J. Grunenberg, *J. Chem. Phys.* **2010**, *132,* 184101.
[80] L. Zhou, S. A. Siegelbaum, *Biophys. J.* **2008**, *94,* 3461.

Received: 23 December 2011
Revised: 9 May 2012
Accepted: 24 June 2012
Published online on 3 September 2012